



Research Article

Performance Evaluation of Grid-Connected Photovoltaic System using SHO-VPTIDF

Satyaprasad Mohapatra ^a, Akshaya Kumar Patra ^{b*}, Debswarup Rath ^a

^a Department of Electrical Engineering, ITER, Siksha 'O'Anusandhan University, Bhubaneswar, P. O. Box: 751030, Odisha, India.

^b Department of Electrical and Electronics Engineering, ITER, Siksha 'O'Anusandhan University, Bhubaneswar, P. O. Box: 751030, Odisha, India.

PAPER INFO

Paper History:

Received: 16 August 2022

Revised: 04 November 2022

Accepted: 24 November 2022

Keywords:

SHO-VPTIDF,
Fault Detection,
Harmonic Mitigation,
Improved Performance,
Enhanced Stability,
Non-Ideal Boost Converter

ABSTRACT

The design of a Spotted Hyena Optimization Algorithm-Variable Parameter Tilt Integral Derivative with Filter (SHO-VPTIDF) controller for improved performance and enhanced devaluation of harmonic components of grid-connected photovoltaic systems is the main objective of the suggested manuscript. The SHO-VPTIDF controller is proposed by reformulating Tilt Integral Derivative Controller with Filter (TIDCF). The TIDCF is characterized by longer simulation time, lower robustness, longer settling time, attenuated ability for noise rejection, and limited use. This research gap is addressed by replacing the constant gains of TIDCF by variable parameter tilt integral derivative with filter. The VPTIDF replaces the constant gains of TIDCF with error varying control parameters to improve the robustness of the system. The photovoltaic system with nonlinearities causes power quality issues and occasional faults, which can be detected by using Levenberg-Marquardt Algorithm (LMA) based machine learning technique. The novelties of the proposed manuscript including improved stability, better robustness, upgraded accuracy, better harmonic mitigation ability, and improved ability to handle uncertainties are verified in a Matlab simulink environment. In this manuscript, the SHO-VPTIDF and the Direct and Quadrature Control based Sinusoidal Pulse Width Modulation (DQCSPWM) method are employed for fault classification, harmonic diminishing, stability enhancement, better system performance, better accuracy, improved robustness, and better capabilities to handle system uncertainties.

<https://doi.org/10.30501/jree.2022.355402.1428>

1. INTRODUCTION

The major components of the SHO-VPTIDF-based photovoltaic system are solar photovoltaic array, non-ideal boost converter, micro inverter, and SHO-VPTIDF controller. The non-ideal boost converter is preferred over conventional boost converter because of its ability to reduce the effects of parasitic capacitance, high efficiency, high power density, lower magnitude of ripple voltage, and lower duty cycle. Insulated-Gate-Bipolar-Transistor (IGBT) is used as a controlled switching device in the proposed boost converter (Sadaf et al., 2020; Hu et al., 2019). However, the boost converters in (Sadaf et al., 2020; Hu et al., 2019) are modeled by state space technique to study the steady-state behavior while ignoring the dynamic behavior. The dynamic modeling of boost converters allows for the impact assessment of all components. Therefore, the modeling technique, though being adequate, fails to be accurate. The SHO-VPTIDF controller is proposed to deliver the triggering pulse to the IGBT used in the proposed non-ideal boost converter. Some of the notable techniques for pulse generation include the extensive use of Phase Locked Loops along with Second Order Generalized Integrators (PLL-SOGI) (Xu et al., 2019; Ahmad & Singh, 2017), Proportional Resonant Controller (PRC) (Keddar et al., 2019; Huang et al., 2018; Sattianadan et al., 2020), Hysteresis

Current Controller (HCC) (Zhao et al., 2018; Zeb et al., 2019), Phase Locked Loop-Feed Forward (PLL-FF) (Wang et al., 2020), and Proportional Integral Derivative Controller (PIDC) (Khan et al., 2019). The major concerns about the above-mentioned control techniques including their effect on the SOGI-PLL with grid voltage variations and the impact of temperature changes were not addressed in (Xu et al., 2019; Ahmad & Singh, 2017). The lingering concerns about the PRC are that it has little control over the generation of accurate control signals and is prone to variation in frequency deviations, which were not investigated in (Keddar et al., 2019; Huang et al., 2018; Sattianadan et al., 2020). The challenges posed by HCC are variable switching frequencies and the impact of having highly electrostatic resistance in the circuit, which were not discussed in (Zhao et al., 2018). The performance of the model in (Zeb et al., 2019; Wang et al., 2020; Khan et al., 2019) was found prone to disturbances due to uncertain convergence time, with reduced stability, reduced efficiency and higher harmonic distortions. SHO-VPTIDF is a variable fractional-order controller. The selection of fractional-order controller is due to its ability to suppress chaotic behavior in scientific models while improving the stability of the system and robustness, thereby exhibiting a superior dynamic response (Patra et al., 2020; Rath et al., 2021; Patra et al., 2022; Tzounas et al., 2020). This proposed controller is the modified form of

*Corresponding Author's Email: akshayapatra@soa.ac.in (A. Kumar Patra)

URL: https://www.jree.ir/article_163319.html



TIDCF. The disparities in research concerning the TIDCF design are rooted in longer simulation time, longer settling time, and attenuated noise rejection ability along with limited usage. The above research gaps are addressed by replacing the TIDC with the proposed approach. The VPTIDF replaces the constant gains of TIDCF with error varying control parameters to improve the robustness of the system. This suggested controller (SHO-VPTIDF) uses a prefilter (N), which is a first-order filter that was chosen due to its ability to improve the controller response, in which case the system would experience less overshoot. The SHO-VPTIDF control parameters are tuned by Spotted Hyena Optimization Algorithm (SHO) to achieved an improved response (Dhiman & Kumar, 2017). The response of the controller is not always optimized in the process of optimizing the control parameters. A system must have a robust controller for it to be considered robust. Consideration of control parameters as variables that change in response to error facilitates achieving robustness. SHO-VPTIDF employs this idea.

A micro inverter receives direct feeding of the DC voltage generated by the boost converter. Low power inverters are known as micro inverters. The foremost advantage of using a micro inverter is that despite poorer proficiency than string inverters, efficacy largely increases due to the freedom with which each inverter unit can operate (Mokhtar et al., 2021; Yaqoob et al., 2021). The performance of micro inverters implemented in (Mokhtar et al., 2021; Yaqoob et al., 2021) facilitates harmonic mitigation and performance improvement under variations in the input parameters. Utilizing a DQCSPWM technique, the micro inverter system is tuned (Chaithanakulwat et al., 2021; Missula & Adda, 2021). By examining the Matignon stability theorem, the stability of the proposed control technique is assessed (Ben Makhoulouf et al., 2020). The measurement of Total Harmonic Distortion (THD) is standardized by IEEE-519 (Marrero et al., 2021; Ben Makhoulouf et al., 2020). All power systems are subject to fault occurrence. Any fault detecting system must be able to distinguish between a healthy system and a malfunctioning one. Fault classification must be used because it enhances system response. Machine learning methods like Levenberg Marquardt Algorithm are used to identify faults (LMA). The ability to detect faults is enhanced by the use of the Levenberg Marquardt Algorithm (LMA). The benefits of control theory, fractional calculus, machine learning based fault detection techniques, and variation in control parameters have never been combined before. Thus, based on inspiration from the concepts mentioned above, a new control technique (SHO-VPTIDF) and fault detection mechanism are proposed for the solar photovoltaic system (Fazai et al., 2019). Since there are no known records on combining the advantages of fractional-order controllers, non-ideal boost converters, micro inverters, and fault prediction ability, the authors of this study have taken this gap as a motivation for further research. This manuscript presents an innovative assimilation of techniques for the enhanced performance and fault prediction of the single-phase photovoltaic system. The novelty of the proposed photovoltaic system includes improved stability, better robustness, upgraded accuracy, better harmonic mitigation ability, and improved ability to handle uncertainties. The suggested single-phase solar photovoltaic system with SHO-VPTIDF provides the following key contributions:

- In order to perform analyze the performance of the photovoltaic model, it is designed in a simulation-based software atmosphere.
- SHO-VPTIDF control strategy with DQCSPWM is formulated for the photovoltaic system to ensure superior performance as well as enhanced devaluation of harmonic.
- Justification for superior performance assessment of harmonic distortions is done in the proposed photovoltaic system.
- Enhancement of robustness, improvement of fault identification ability, noise reduction ability of the SHO-VPTIDF-based photovoltaic system are provided.
- The superior performance of the SHO-VPTIDF-based photovoltaic system is validated by performing a relative exploration with prevalent practices.

The rest of the manuscript is structured as follows. Section 2 present the mathematical modeling of photovoltaic cell, non-ideal boost converter, DQCSPWM, and micro inverter as well as open-loop analysis of the SHO-VPTIDF-based photovoltaic system. Section 3 presents the mathematical modeling of SHO-VPTIDF. Section 4 gives the analysis result as well as the validation of the improved performance and robustness. Section 5 presents the concluding remarks.

2. PROBLEM FORMULATIONS

The major components of the proposed photovoltaic system are photovoltaic cell, DQCSPWM triggering mechanisms, micro inverter, SHO-VPTIDF, and converter. Figure 1(a) depicts a framework of the proposed photovoltaic system. However, Figure 1(b) to (d) shows the simulation model of the proposed non-ideal boost converter along with photovoltaic cell. Figure 1(e) presents the working simulation model of the PV system. The appending sections show extensive modeling of the photovoltaic system.

2.1. Solar array

The inputs to the solar array are solar irradiance and temperature. The mathematical relationship among the overall output current generated by the photovoltaic cell (I_t), voltage across the photovoltaic diode (V_{dt}), reverse saturation current (I_{rs}), photo current (I_{photo}), charge of an electron (q_c), Boltzmann coefficient (k), diode ideality factor (d_{if}), and temperature (T) in $^{\circ}K$ are represented by Equation (1). The characteristics of solar photovoltaic cell consisting of several solar photovoltaic cells can be mathematically expressed by Equation (2).

$$I_t = I_{photo} - I_{rs} \left[\exp\left(\frac{q_c V_{dt}}{akT}\right) \right] \quad (1)$$

$$I_t = \frac{R_{leakage}}{R_{series} + R_{leakage}} \left(I_{photo} - I_{rs} \left[\exp\left(\frac{V_{dt} + R_{series}}{d_{if} V_{ter}}\right) - 1 \right] \left(\frac{V_{dt}}{R_{leakage}} \right) \right) \quad (2)$$

where I_t is overall output current, I_{photo} photo current, I_{rs} the reverse saturation current, T temperature in $^{\circ}K$, d_{if} diode ideality factor, q_c charge of electron, R_{series} series resistance,

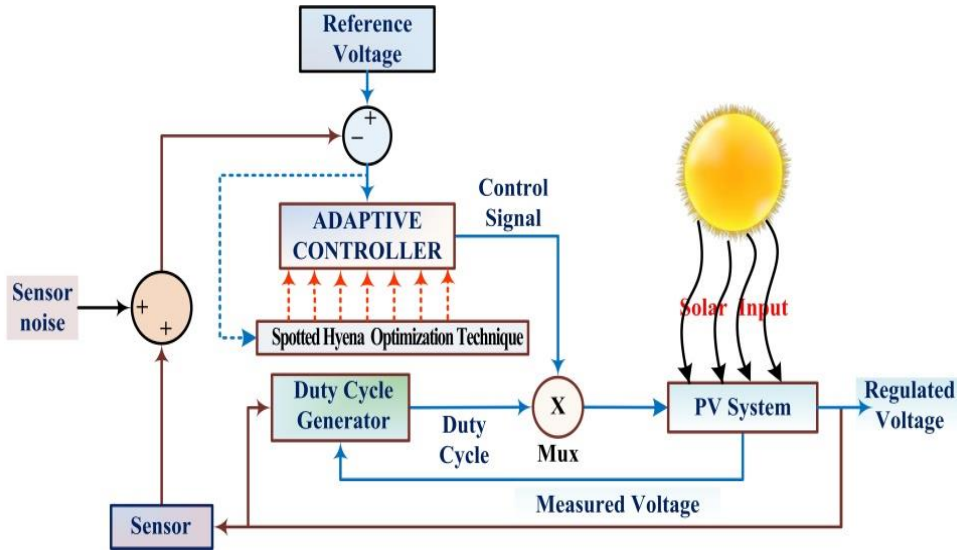
$R_{leakage}$ shunt resistance, V_{ter} nominal terminal voltage, k Boltzmann constant, and v_{dt} the voltage across the diode. In the ideal condition, it is assumed that $I_{Short} \gg I_{Photo}$ and is validated because $R_{leakage}$ exceeds R_{Series} . The current through diode, I_{photo} , has dependencies on temperature and solar irradiance irr . This is established by Equation (3) and I_{rs} is represented in Equation (4).

$$I_{photo} = \left(\frac{R_{Series} + R_{leakage}}{R_{leakage}} I_{Short} + K_{sct} T_c \right) \frac{irr}{irr_n} \quad (3)$$

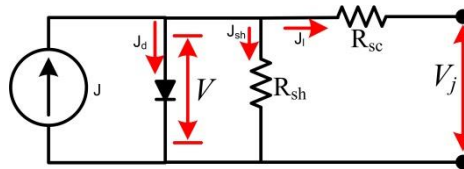
$$I_{rs} = \frac{I_{Short} + K_{sct} T_c}{\exp\left(\frac{V_{Open} + K_{vtc} T_c}{d_{if} V_{ter}}\right) - 1} \left(\frac{T_{nom}}{T}\right)^3 \exp\left[\frac{q_c E_{bg}}{d_{if} k} \left(\frac{1}{T_{nom}} - \frac{1}{T}\right)\right] \quad (4)$$

where K_{sct} is short-circuit temperature, K_{vtc} voltage / temperature coefficient, T_c change in temperature in $^{\circ}K$, irr_n solar nominal irradiation in KW/m^2 , E_{bg} band gap energy, T_{nom} the nominal temperature. 1.3 is the magnitude of identity factor of diode. Upon substitution of Equation (3) to (4) in Equation (1), the modified expression is mediated via Equation (5).

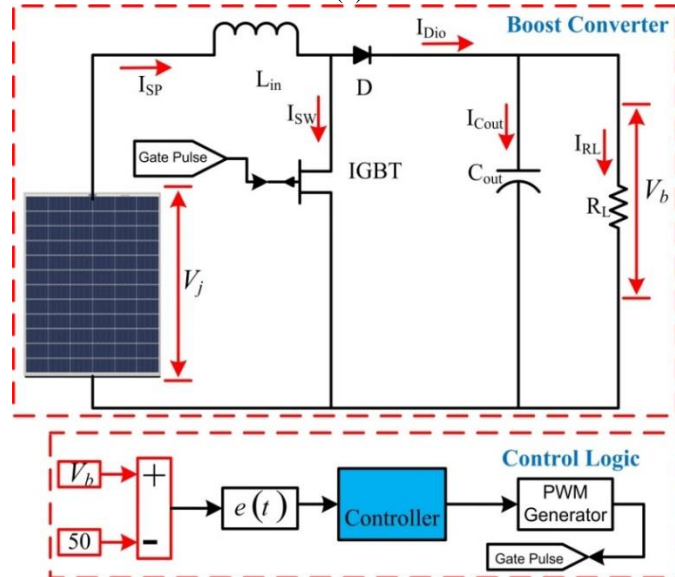
$$I_t = \frac{R_{leakage}}{R_{Series} + R_{leakage}} \left(I_{photo} - I_{rs} \left[\exp\left(\frac{V_{dt} + R_{Series}}{d_{if} V_{ter}}\right) - 1 \right] \left(\frac{V_{dt}}{R_{leakage}} \right) \right) \quad (5)$$



(a)



(b)



(c)

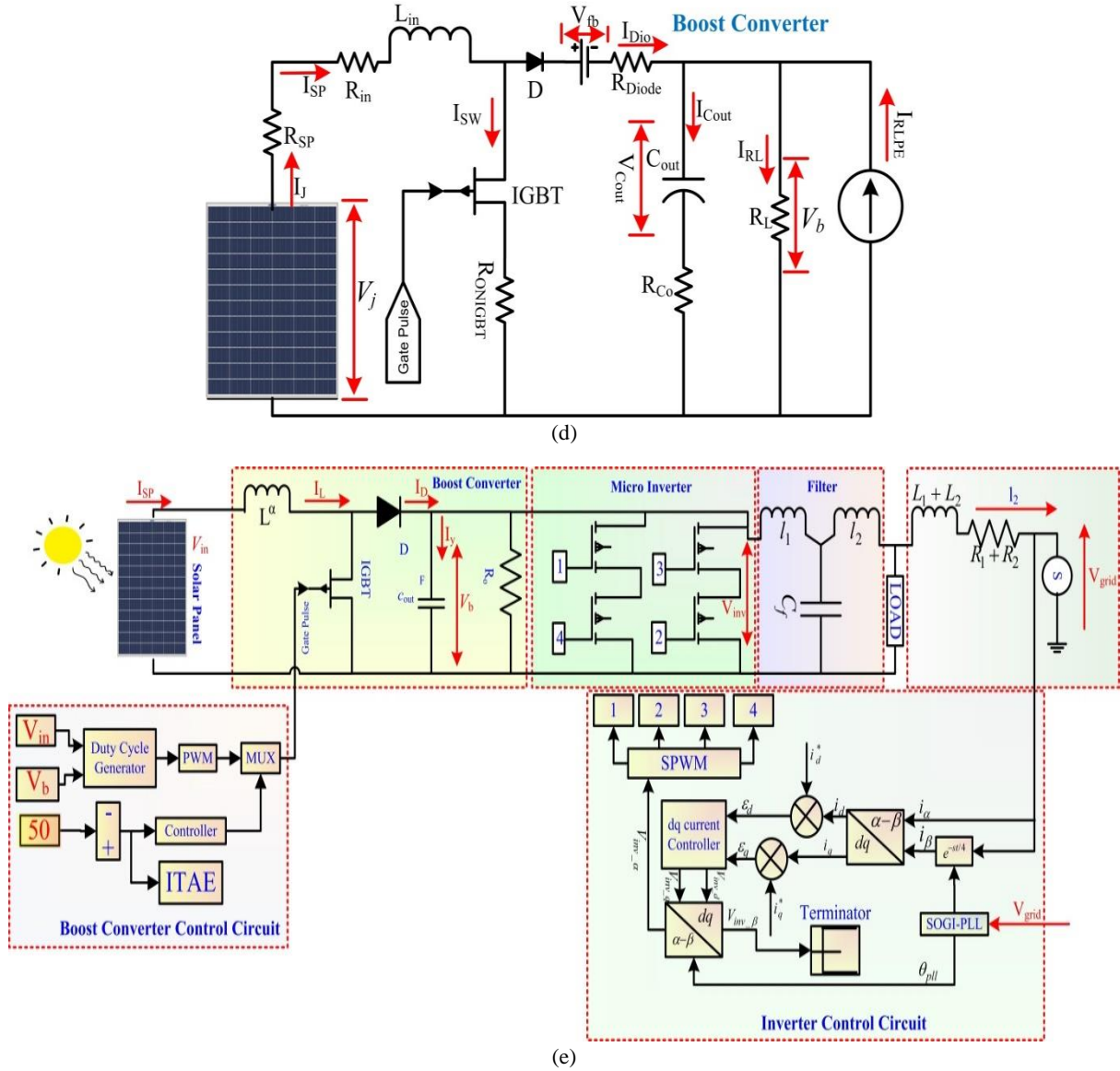


Figure 1. (a) Schematics of SHO-VPTIDF-based photovoltaic system, (b) mathematical model of solar cell, (c) idealistic model of boost converter, (d) exact model of non-ideal model boost converter, (e) simulation model of SHO-VPTIDF-based photovoltaic system

2.2. Boost converter

The inputs from photovoltaic panels are of low magnitude (in the range of 20 to 25 volts). This low-magnitude voltage finds little to no use when inverted to AC directly. Therefore, there is a need for boost converter. The boost converter is modeled in the scope of this study by considering the impacts of parasitic components and equivalent resistance of all components. The idealistic boost converter is depicted in Figure 1 (b), while Figure 1 (c, d) represents approximate and exact Non-ideal Boost Converter (NBC) models. The NBC is modeled via the state space averaging technique, given that the state space averaging technique contributes to the study of steady state and dynamic behaviors.

2.2.1. Non-ideal boost converter

The main components of NBC include one insulated gate bipolar transistor (IGBT), one diode (D), and each of inductor and capacitor (L_{in} and C_{out}). The internal resistance of the photovoltaic array is denoted by R_{SP} . Equivalent Series Resistance (ESR) of IGBT, D, L_{in} and C_{out} is represented by R_{ONIGBT} , R_{Diode} , R_{lin} , and R_{Co} , respectively. V_{fb} represents

the forward voltage drop of D. The value of ESR is typically less than 1Ω . The operating period of NBC is alienated into two parts: IGBT on period and IGBT off period (Xu et al., 2019).

2.2.1.1. IGBT on

I_t represents the current received from the photovoltaic array. The voltage from solar panels is represented by V_{ter} . Equation (6) represents the exciter loop equation.

$$L_{in} \frac{dI_t}{dt} = -(R_{lin} + R_{ONIGBT} + R_{SP})I_t + V_{ter} \quad (6)$$

To study the NBC, a small perturbation current (I_{RLPE}) is applied by C_{out} . It is expressed as a component of current of C_{out} ($I_{Cout}(t)$). $I_{Cout}(t)$ is expressed mathematically by Equation (7).

$$I_{Cout}(t) = \frac{C_{out}dV_{Cout}(t)}{dt} = \frac{(R_L \parallel R_{Co})}{(R_L + R_{Co})} V_{Cout}(t) - \frac{(R_L \parallel R_{Co})}{R_{Co}} I_{RLPE}(t) \quad (7)$$

The output voltage ($V_b(t)$) is represented by Equation (8).

$$V_b(t) = \frac{(R_L \parallel R_{Co})}{(R_{Co})} V_{Cout}(t) - (R_L \parallel R_{Co}) I_{RLPE}(t) \quad (8)$$

The state space equation is represented by Equation (9).

$$\begin{cases} \dot{z}_2(t) = A_{IGBTON} z_2(t) + B_{IGBTON} u(t) + G_{IGBTON} V_{fb} \\ y(t) = C_{IGBTON} z_2(t) + E_{IGBTON} u(t) + H_{IGBTON} V_{fb} \end{cases} \quad (9)$$

The state space matrices (A_{IGBTON} , B_{IGBTON} , C_{IGBTON} , E_{IGBTON} , G_{IGBTON} , and H_{IGBTON}) are represented below.

$$A_{IGBTON} = \begin{bmatrix} \frac{-(R_{ONIGBT} + R_{in} + R_{SP})}{L_{in}} & 0 \\ 0 & \frac{(R_L \parallel R_{Co})}{(C_{out} R_L R_{Co})} \end{bmatrix};$$

$$B_{IGBTON} = \begin{bmatrix} \frac{1}{L_{in}} & 0 \\ 0 & \frac{(R_L \parallel R_{Co})}{(C_{out} R_{Co})} \end{bmatrix}; C_{IGBTON} = \begin{bmatrix} 0 & \frac{(R_L \parallel R_{Co})}{(R_{Co})} \\ 1 & 0 \end{bmatrix};$$

$$E_{IGBTON} = \begin{bmatrix} 0 & -(R_L \parallel R_{Co}) \\ 0 & 0 \end{bmatrix}; G_{IGBTON} = \begin{bmatrix} 0 & 0 \end{bmatrix}^T;$$

$$H_{IGBTON} = \begin{bmatrix} 0 & 0 \end{bmatrix}^T$$

2.2.1.2. IGBT off

$V_{Cout}(t)$ denotes the voltage across C_{out} . After switching off IGBT and successfully triggering D, the working equation of NBC is expressed mathematically by Equation (10).

$$L_{in} \frac{dI_t}{dt} = -((R_L + R_{Diode} + R_{SP}) + (R_L \parallel R_{Cout})) I_t - \frac{(R_L \parallel R_{Cout})}{R_{Cout}} V_{Cout}(t) + V_{ter} + (R_L \parallel R_{Cout}) I_{RLPE}(t) - V_{fb} \quad (10)$$

The expression for $I_{Cout}(t)$ is denoted in Equation (11).

$$I_{Cout}(t) = \frac{C_{out} dV_{Cout}(t)}{dt} = \frac{(R_L \parallel R_{Co})}{(R_{Co})} I_{RL}(t) - \frac{(R_L \parallel R_{Co})}{R_L R_{Co}} V_{Cout}(t) - \frac{(R_L \parallel R_{Co})}{(R_{Co})} I_{RLPE}(t) \quad (11)$$

$V_b(t)$ due to triggering of D is expressed mathematically by Equation (12).

$$V_b = \frac{(R_L \parallel R_{Co})}{(R_{Co})} V_{Cout}(t) - (R_L \parallel R_{Co}) I_{RLPE}(t) + (R_L \parallel R_{Co}) I_{RL}(t) \quad (12)$$

Utilizing Equations (10) to (12), the state variables for the triggering of D are expressed by Equations (13) to (14).

$$z_2(t) = \begin{bmatrix} I_t & V_{Cout}(t) \end{bmatrix}^T, u(t) = \begin{bmatrix} V_b & I_{RLPE}(t) \end{bmatrix}^T \text{ and}$$

$$y(t) = \begin{bmatrix} V_b(t) & I_J(t) \end{bmatrix}^T$$

$$\dot{z}_2(t) = A_{IGBTOFF} z_2(t) + B_{IGBTOFF} u(t) + G_{IGBTOFF} V_{fb} \quad (13)$$

$$y(t) = C_{IGBTOFF} z_2(t) + E_{IGBTOFF} u(t) + H_{IGBTOFF} V_{fb} \quad (14)$$

The state space matrices ($A_{IGBTOFF}$, $B_{IGBTOFF}$, $C_{IGBTOFF}$, $E_{IGBTOFF}$, $G_{IGBTOFF}$, and $H_{IGBTOFF}$) are given below.

$$A_{IGBTOFF} = \begin{bmatrix} \frac{-(R_{Diode} + R_{SP} + R_L) + ((R_L \parallel R_{Co}))}{L_{in}} & 0 \\ 0 & \frac{(R_L \parallel R_{Co})}{(C_{out} R_L R_{Co})} \end{bmatrix};$$

$$B_{IGBTOFF} = \begin{bmatrix} \frac{1}{L_{in}} & \frac{(R_L \parallel R_{Co})}{L_{in}} \\ 0 & \frac{(R_L \parallel R_{Co})}{(C_{out} R_{Co})} \end{bmatrix}; C_{IGBTOFF} = \begin{bmatrix} (R_L \parallel R_{Co}) & \frac{(R_L \parallel R_{Co})}{(R_{Co})} \\ 1 & 0 \end{bmatrix};$$

$$E_{IGBTOFF} = \begin{bmatrix} 0 & -(R_L \parallel R_{Co}) \\ 0 & 0 \end{bmatrix}; G_{IGBTOFF} = \begin{bmatrix} -1 \\ L_{in} \end{bmatrix}^T; H_{IGBTOFF} = \begin{bmatrix} 0 & 0 \end{bmatrix}^T$$

Through Equation (8-13), the expression for the state space matrices (A_{tot} , B_{tot} , C_{tot} , E_{tot} , G_{tot} and H_{tot}) is represented below.

$$\left. \begin{aligned} A_{tot} &= D_y A_{IGBTON} + \tilde{D}_y A_{IGBTOFF}; B_{tot} = D_y B_{IGBTON} + \tilde{D}_y B_{IGBTOFF}; \\ C_{tot} &= D_y C_{IGBTON} + \tilde{D}_y C_{IGBTOFF}; E_{tot} = D_y E_{IGBTON} + \tilde{D}_y E_{IGBTOFF}; \\ G_{tot} &= D_y G_{IGBTON} + \tilde{D}_y G_{IGBTOFF}; H_{tot} = D_y H_{IGBTON} + \tilde{D}_y H_{IGBTOFF} \end{aligned} \right\}$$

where the expressions D_y and $\tilde{D}_y = 1 - D_y$ represent duty cycle and opposite of duty cycle, respectively. The expression of state matrices is expressed below.

$$A_{tot} = \begin{bmatrix} \frac{-((D R_{ONIGBT} + \tilde{D} R_{Diode} + R_{SP} + R_{in}) (R_L + R_{Cout}) + D \tilde{D} R_L R_{Co})}{L_{in}} & \frac{\tilde{D} (R_L \parallel R_{Co})}{(L_{in} R_{Co})} \\ \frac{\tilde{D} (R_L \parallel R_{Co})}{(C_{out} R_{Co})} & \frac{(R_L \parallel R_{Co})}{(C_{out} R_L R_{Co})} \end{bmatrix};$$

$$B_{tot} = \begin{bmatrix} \frac{1}{L_{in}} & \frac{\tilde{D} (R_L \parallel R_{Co})}{L_{in}} \\ 0 & \frac{(R_L \parallel R_{Co})}{(C_{out} R_{Co})} \end{bmatrix}; C_{tot} = \begin{bmatrix} \tilde{D} (R_L \parallel R_{Co}) & \frac{(R_L \parallel R_{Co})}{(R_{Co})} \\ 1 & 0 \end{bmatrix}; E_{tot} = \begin{bmatrix} 1 & -(R_L \parallel R_{Co}) \\ 0 & 0 \end{bmatrix};$$

$$G_{tot} = \begin{bmatrix} \tilde{D} \\ L_{in} \\ 0 \end{bmatrix}; H_{tot} = \begin{bmatrix} 0 \\ 0 \end{bmatrix}$$

The transfer function ($G(s)$) for the NBC is obtained after performing small signal analysis and is expressed mathematically via Equation (15).

$$G(s) = \frac{V_b}{V_{ter}} = C_{tot} (sI - A_{tot})^{-1} B_{tot} + E_{tot} \quad (15)$$

where the unitary matrix and laplace operator are represented by I and s, respectively.

2.3. Micro inverter

$V_b(t)$ from NBC is converted into alternating quantity using micro inverter. The foremost advantages of using low-power micro inverters are improved effectiveness, improved safety, no single-point failure, and scope for future expansion. The micro inverters have lower proficiency than string inverters, but the ability of individual inverters to act freely sets poles apart (Mokhtar et al., 2021; Yaqoob et al., 2021). The scope of future expansion of micro inverters is wider and easier to implement. Micro inverter systems are flexibly modifiable as power demands increase or decrease over time. In contrast, the size of

a string-based inverter should be determined by the maximum power. When future growth is anticipated, it is possible to choose a larger than usual string inverter, but doing so for an uncertain future raises costs regardless. Since many micro inverter manufacturers provide applications or websites to check their products, checking and maintenance are also made simpler. DQCSPWM is used to trigger the switches in the micro inverter system.

2.3.1. Harmonic

The measure of all components of harmonic present in an electrical current signal is termed as the total harmonic distortion. The extensive use of power electronic-based switches leads to the induction of harmonic distortions in electrical signals. It is represented symbolically by i_{thd} . Numerous potential avenues exist for harmonics to impact electricity systems. Moreover, the mentioned impact results in the unnecessary tripping of circuit breakers, reduced power factors, higher heat generation, reduced efficiency, and increased electromagnetic emissions. It is out intention to maintain the low value of i_{thd} as it reduces peak current, improves power factor, and efficiency. The standard for measuring i_{thd} is provided by IEEE-519 (Marrero et al., 2021).

2.4. Direct and quadrature control-based sinusoidal pulse width modulation (DQCSPWM)

In order to design the proposed switching strategy, a computational model of the SHO-VPTIDF-based photovoltaic system is used (Chaithanakulwat et al., 2021; Missula & Adda, 2021). The voltage and current from grid are represented by V_{grid} and i_2 , respectively. The voltage and current from micro inverter are represented by V_{inv} and i_1 , respectively. Micro inverter and grid are interconnected via a filter. The resistance and inductance of the inverter side are represented by R_1 and L_1 , respectively. The resistance and inductance of the grid side are represented by R_2 and L_2 . The coupling capacitance is represented by C_f . The combined dynamic equation of the grid and inverter is represented by Equations (16-18).

$$V_{inv} = R_1 i_1 + sL_1 i_1 + V_{cf} \quad (16)$$

$$V_{cf} = R_2 i_2 + sL_2 i_2 + V_{grid} \quad (17)$$

$$i_1 = i_2 + \frac{V_{cf}}{S} \quad (18)$$

The components α and β of V_{inv} are represented by V_{inv_alpha} and V_{inv_beta} , respectively. The impact of C_f can be neglected while designing the current controller. Thus, Equation (16) is revised and expressed in $\alpha\beta$ frame, as represented by Equations (19-20).

$$V_{inv_alpha} = (R_1 + R_2) i_{alpha} + s(L_1 + L_2) i_{alpha} + V_{grid_alpha} \quad (19)$$

$$V_{inv_beta} = (R_1 + R_2) i_{beta} + s(L_1 + L_2) i_{beta} + V_{grid_beta} \quad (20)$$

where i_α and i_β are expressed by Equation (21).

$$\left. \begin{aligned} i_\alpha &= i = I_m \cos(\theta) \\ i_\beta &= i = I_m \sin(\theta) \end{aligned} \right\} \quad (21)$$

In order to simplify the computations, Equations (19-20) in the stationary reference frame are transformed into a rotating reference frame represented by Equation (30).

$$\left. \begin{aligned} V_{inv_d} &= (R_1 + R_2) i_d + s(L_1 + L_2) i_d - \omega_{ff} (L_1 + L_2) i_q + V_{grid_d} \\ V_{inv_q} &= (R_1 + R_2) i_q + s(L_1 + L_2) i_q - \omega_{ff} (L_1 + L_2) i_d + V_{grid_q} \end{aligned} \right\} \quad (22)$$

ω_{ff} represents the nominal angular frequency. The relationship between V_{inv} , V_{grid} and the voltage control signals (V_{c_d} and V_{c_q}) of dq axis is expressed by Equation (23).

$$\left. \begin{aligned} V_{inv_d} &= V_{c_d} - \omega_{ff} (L_1 + L_2) i_q + V_{grid_d} \\ V_{inv_q} &= V_{c_q} - \omega_{ff} (L_1 + L_2) i_d + V_{grid_q} \end{aligned} \right\} \quad (23)$$

V_{c_d} and V_{c_q} are used to calculate i_d and i_q . They are mathematically expressed by Equation (24).

$$\left. \begin{aligned} V_{c_d} &= (R_1 + R_2) i_d + s(L_1 + L_2) i_d \\ V_{c_q} &= (R_1 + R_2) i_q + s(L_1 + L_2) i_q \end{aligned} \right\} \quad (24)$$

The minimum number of variables required for single-phase $\alpha\beta$ to dq transformation is two. Hence, in order to undergo $\alpha\beta$ to dq transformation, a friction variable (i_α^* and i_β^*) is created.

The mathematical equivalence for i_α^* and i_β^* is expressed by Equation (25).

$$\left. \begin{aligned} i_\alpha^* &= I_m^* \cos(\theta_{PLL}) \\ i_\beta^* &= I_m^* \sin(\theta_{PLL}) \end{aligned} \right\} \quad (25)$$

This friction component is the phase shifted version of the original measured signal. The expression for $\alpha\beta$ to dq transformation and vice versa is expressed by Equations (26-27), respectively.

$$\begin{bmatrix} \alpha \\ \beta \end{bmatrix} = \begin{bmatrix} \cos(\theta) & -\sin(\theta) \\ \sin(\theta) & \cos(\theta) \end{bmatrix} \begin{bmatrix} d \\ q \end{bmatrix} \quad (26)$$

$$\begin{bmatrix} d \\ q \end{bmatrix} = \begin{bmatrix} \cos(\theta) & \sin(\theta) \\ -\sin(\theta) & \cos(\theta) \end{bmatrix} \begin{bmatrix} \alpha \\ \beta \end{bmatrix} \quad (27)$$

The application of dq transformation with $\theta=\theta_{PLL}$ in the two reference currents (i_d^* and i_q^*) is expressed in Equation (28).

$$\left. \begin{aligned} i_d^* &= I_m^* \left(\cos^2(\theta_{PLL}) + \sin^2(\theta_{PLL}) \right) = I_m^* \\ i_q^* &= I_m^* \left(-\cos(\theta_{PLL}) \cdot \sin(\theta_{PLL}) + \sin(\theta_{PLL}) \cdot \cos(\theta_{PLL}) \right) = 0 \end{aligned} \right\} \quad (28)$$

The insertion of delay makes the system response slower. This slow response of the system is addressed by using error signal ($i_\alpha^* - i_\alpha$) to generate the error (steady state) in the dq frame. Let ε_d and ε_q be the errors for d-axis (direct axis) and q-axis (quadrature axis), respectively. It is assumed that under steady state conditions, $i_\beta - i_\beta^*$. The expression for ε_d and ε_q is represented by Equations (29-30).

$$\left. \begin{aligned} \varepsilon_d &= i_d^* - i_d \\ \varepsilon_d &= \left[i_\alpha^* \cos(\theta_{PLL}) + i_\beta^* \sin(\theta_{PLL}) - i_\alpha \cos(\theta_{PLL}) + i_\beta \sin(\theta_{PLL}) \right] \\ \varepsilon_d &= \left[(i_\alpha^* - i_\alpha) \cos(\theta_{PLL}) + (i_\beta^* - i_\beta) \sin(\theta_{PLL}) \right] \\ \varepsilon_d &= \left[(i_\alpha^* - i_\alpha) \cos(\theta_{PLL}) \right] \\ \varepsilon_q &= i_q^* - i_q \\ \varepsilon_q &= \left[-i_\alpha^* \sin(\theta_{PLL}) + i_\beta^* \cos(\theta_{PLL}) - i_\alpha \sin(\theta_{PLL}) + i_\beta \cos(\theta_{PLL}) \right] \\ \varepsilon_q &= \left[-(i_\alpha^* - i_\alpha) \sin(\theta_{PLL}) + (i_\beta^* - i_\beta) \cos(\theta_{PLL}) \right] \\ \varepsilon_q &= \left[-(i_\alpha^* - i_\alpha) \sin(\theta_{PLL}) \right] \end{aligned} \right\} \quad (29)$$

$$\left. \begin{aligned} \varepsilon_q &= i_q^* - i_q \\ \varepsilon_q &= \left[-i_\alpha^* \sin(\theta_{PLL}) + i_\beta^* \cos(\theta_{PLL}) - i_\alpha \sin(\theta_{PLL}) + i_\beta \cos(\theta_{PLL}) \right] \\ \varepsilon_q &= \left[-(i_\alpha^* - i_\alpha) \sin(\theta_{PLL}) + (i_\beta^* - i_\beta) \cos(\theta_{PLL}) \right] \\ \varepsilon_q &= \left[-(i_\alpha^* - i_\alpha) \sin(\theta_{PLL}) \right] \end{aligned} \right\} \quad (30)$$

Equations (24-38) are applied to generate a sinusoidal reference for the Sinusoidal Pulse With Modulation (SPWM). The intersection between the sinusoidal reference and the square carrier wave determines the operating states of DQCSPWM. When the magnitude of reference wave (V_c) exceeds that of carrier wave (V_{car}), the positive pulse is generated. While the negative pulse is generated if V_{car} exceeds V_c . The modulation index and output voltage (V_{inv}) of the micro inverter are expressed mathematically by Equations (31) to (32).

$$m_a = \frac{V_c}{V_{car}} \quad (31)$$

$$V_{inv} = V_s \sqrt{\left(\frac{2n}{\sum_{b=1}^n} \frac{2T_{on}}{T \times \pi} \right)} \quad (32)$$

where T_{on} is the width of the n^{th} pulse and T is the total time period. The switching scheme is formulated by using Equations (16-32). Figure 1 contains the switching strategy (DQCSPWM) used to trigger the switches present in the micro inverter.

2.5. Filter

Harmonic components exist in signals coming from the micro inverter. These gratuitous signals are removed by using LCL filter. The base impedance (Z_b), base capacitance (C_f), and maximum value of load current (I_{max}) for the LCL filter are expressed in Equations (33) to (35).

$$Z_b = V_b^2 P_1^{-1} \quad (33)$$

$$C_b = (\omega_g Z_b)^{-1} \quad (34)$$

$$I_{max} = 0.333 * P \sqrt{2} * (V_f)^{-1} \quad (35)$$

where P_1 and V_f represent active power and filter voltage, respectively. In order to achieve robustness in the filter design, a tolerance of 10 % is allowed in the values of the filter components. Inverter side inductance (L_1) and change in load current allowing a change of 10 % are represented by Equations (36) to (37).

$$L_1 = \frac{V_b}{0.6 \times f_{sw} \times I_{max}} \quad (36)$$

$$\Delta I_{max} = 0.10 \times I_{max} \quad (37)$$

where f_{sw} and V_b represent the switching frequency and DC link voltage, respectively. The grid side inductor (L_2) and the filter capacitor (C_f) are represented by Equations (38) to (39), respectively.

$$L_2 = \frac{\sqrt{(k_a^{-2} + 1)}}{C_f \times (f_{sw})^2} \quad (38)$$

$$C_f = 0.1 \times C_b \quad (39)$$

where k_a represents the attenuation factor. Electromagnetic interferences and ripple effects are compensated by the use of resistance (R_f) alongside C_f . Equation (40) expresses the mathematical equivalence for R_f .

$$R_f = (3C_f \times \omega_{res})^{-1} \quad (40)$$

where ω_{res} represents angular resonant frequency. Equation (3) helps to establish the filtering strategy for the photovoltaic system and is depicted in Figure 1.

2.6. Fault classification

A fault can be broadly defined as an abnormal working situation. Faults based on clearance time can be divided into two types: small duration faults and long duration faults. The former are typically voltage sag faults and last for anywhere between 5 and 12 cycles. The latter faults are mostly cleared by 30 cycles. Neural networks based on machine learning are trained to distinguish among eight different operating conditions. Grid open circuit faults, grid short circuit faults, load open circuit faults, load short circuit faults, inverter open

circuit faults, inverter device faults, and converter device faults are the faults that are taken into consideration in line with the purposes of this manuscript. Seven different fault types and typical operating conditions are included in the operating conditions. The inputs to the fault classifier are the RMS values of load current as denoted by i_{load} , grid current i_{grid} , inverter current i_{inv} , load voltage V_{load} , grid voltage V_{grid} , inverter voltage V_{inv} , irradiance denoted by irr , Frequency $freq$, temperature T , boost converter output voltage V_b , boost converter output current i_b , total harmonic distortion i_{thd} , solar panel voltage V_t , and solar panel current i_t . A neural network is trained to recognize different types of faults that occur in a photovoltaic system as part of the fault classification mechanism, which is based on machine learning techniques. A Feed-Forward Neural Network (FFNN) is used by the LMA to realize faults. In an FFNN-based ANN, loops do not form. Information travels through the input node to the hidden nodes and, then, to the output node. In the hidden layer, the mathematical optimization is completed. Data preparation and preprocessing are also done in the hidden layer. FNN-based ANN is implemented by the aid of twenty-two hidden layers, three outputs, and fourteen inputs (Fazai et al., 2019).

2.6.1. Levenberg-Marquardt Algorithm (LMA)

Levenberg-Marquardt Algorithm (LMA), a machine learning-based algorithm, is used as a fault detection algorithm. LMA employs computing gradient and Jacobian matrix techniques for quicker and efficient fault tracking. LMA is effectively lowering the values of the cost function (f). The mathematical expression for the cost function is given in Equation (41).

$$f = \sum_{i=1}^m e_i^2 \quad (41)$$

where m characterizes the number of data samples. This performance fails to optimize quickly, hence, the cost function is re-modified and represented by Equation (42).

$$f = \sum_{peak=1}^m t_{peak} * |e_{peak}| \quad (42)$$

Equation (43) expresses the relationship among Jacobian matrix, error vector, and parameter vector. The error vector and parameter vector are represented by e_i and w_j , respectively.

$$J_{i,j} = \frac{\partial e_i}{\partial w_j} \quad (43)$$

where i and j represent instances of a dataset and number of parameters, respectively. The gradient vector Δf and Hessian approximation H_f are used for generating the slope of the vector field and local minima and maxima points. The mathematical expression for Δf and H_f is given by Equation (44).

$$\Delta f = 2j^T .e; \quad H_f \approx 2j^T .j + \lambda I; \quad (44)$$

where λ and I represent damping factor and identity matrix, respectively. An increase in λ causes the iterations to fail, while a decrease in λ value is associated with the improved cost function optimization. This, in turn, speeds up the iterations. The expression for the next set of weights ($w^{(i+1)}$) used for determining the progress of LMA is given in Equation (45).

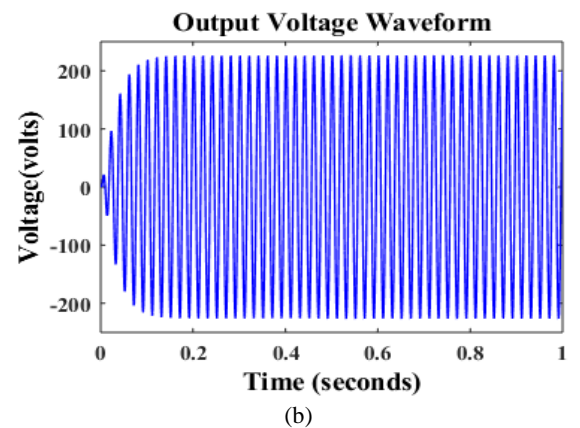
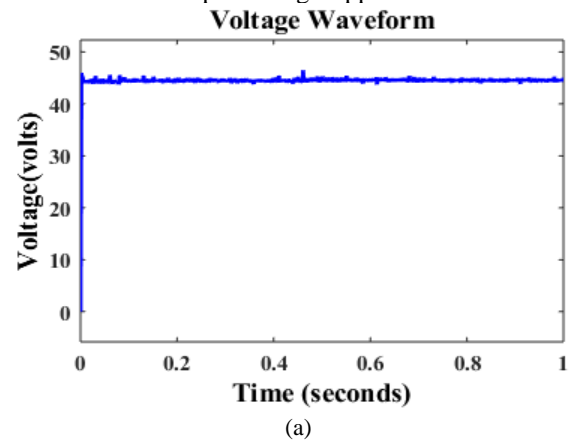
$$w^{(i+1)} = w^i - (j^{(i)T} .j^{(i)} + \lambda I)^{-1} .(2j^{(i)T} .e^{(i)}) \quad (45)$$

2.7. Open-loop response

Supervising sub-sections deliberate upon the characteristics of the solar photovoltaic system, which are investigated under varied operational settings.

2.7.1. Open-loop mode for NBC

The converter used in this manuscript uses IGBT that is pulsed at 30 KHz, and a simple pulse generator is used for triggering IGBTs. The boost converter steps up the voltage from 24 volts from the solar subsystem to 44.48 volts with a ripple of 1.02 volts. Figure 2(a) represents the output voltage of the boost converter at an open loop where the magnitude of the voltage fluctuation ranges between 43.98 volts and 45 volts. The nonlinearities found in photovoltaic systems are the primary reasons behind the output voltage ripples.



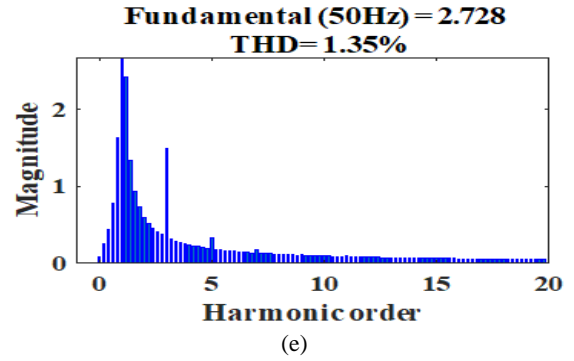
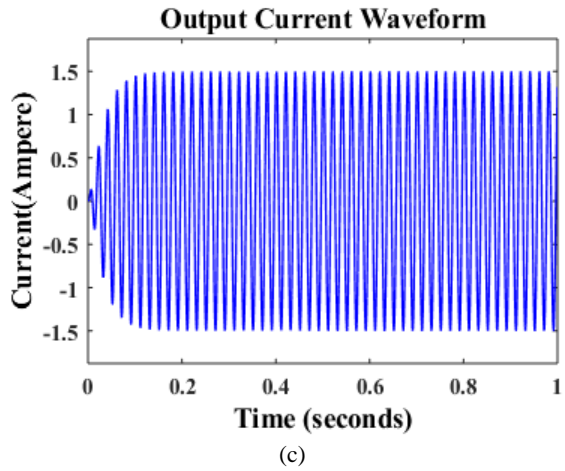
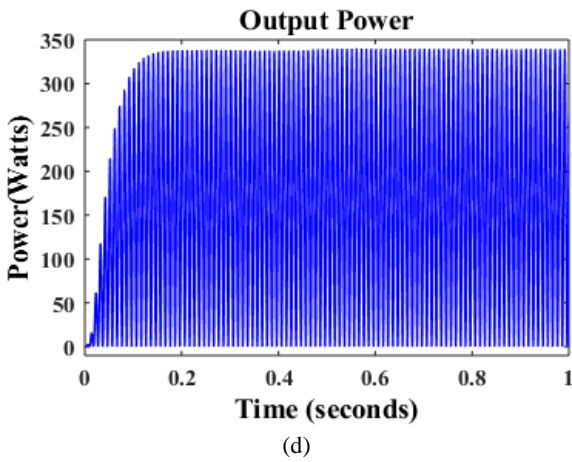


Figure 2. Parameters of open-loop photovoltaic system: (a) Voltage output of NBC, (b) Open-loop micro inverter voltage output, (c) Output current of open-loop micro inverter, (d) Output power of open-loop micro inverter, (e) i_{thd} plot



2.7.2. Open-loop micro inverter

The pulse generator provides 30 KHz switching frequency for the switches present in the micro inverter. The output voltage (V_{inv}) of the micro inverter is 226 volts, the alternating current (i_{inv}) of the inverter is 1.5 ampere, and the apparent power (P_{inv}) of the inverter is 340 watts, as represented in Figure 2(b-d). Figure 2(e) signifies the current harmonic distortion (i_{thd}) found at 1.63%. The open-loop result exploration suggested the application of a control technique.

2.7.3. Open-loop fault analysis

The open-loop system is subjected to the converter device fault at 0.2 second, load fault at 0.3 second, inverter device fault at 0.4 second, and grid fault at 0.5 second. The impact of fault on the open-loop system is evident in Figure 3. The open-loop system fails to recover from the impact of fault. Based on the open-loop analysis, using a control strategy for achieving better outcome is recommended.

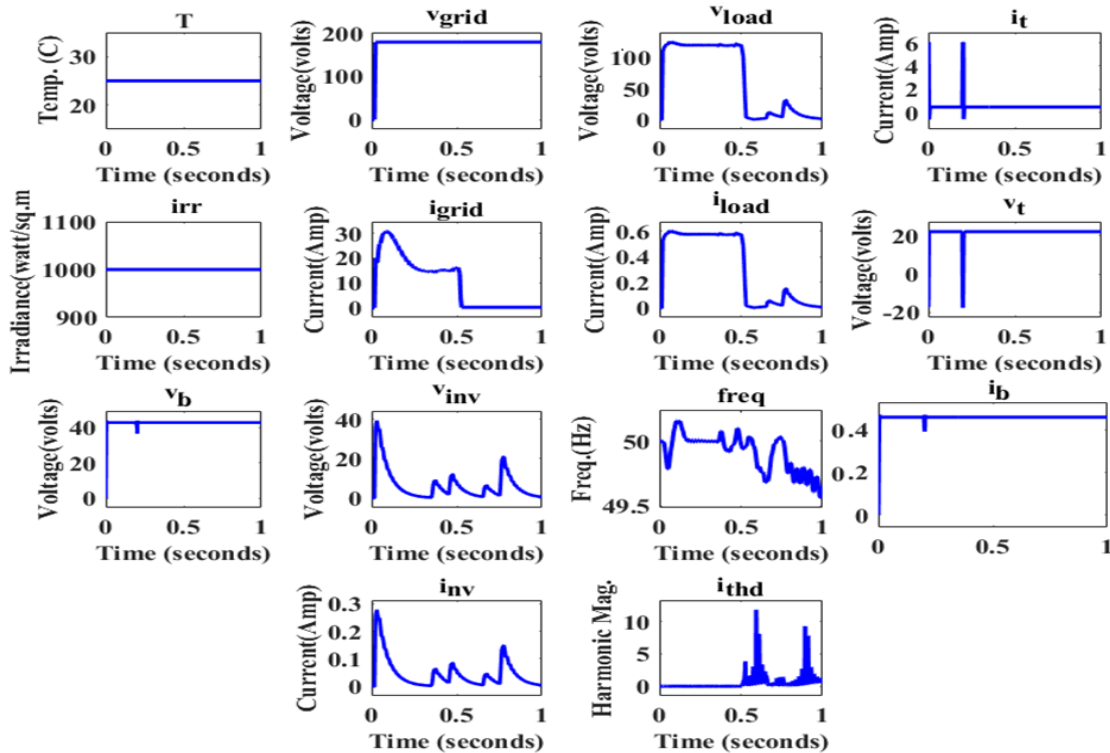


Figure 3. Fault analysis of the open-loop system

3. CONTROL ALGORITHM

In this section, SHO-VPTIDF is discussed in detail. The performance of the SHO-VPTIDF controller-based photovoltaic system in terms of stability, accuracy, and robustness is studied. The controller performance indices such as i_{thd} , V_{inv} , i_{nv} , P_{inv} , and V_b are accessed and analyzed with appropriate justification for the controller performance (Dhiman & Kumar, 2017). SHO-VPTIDF stands defined in the appending sub-sections.

3.1. SHO-VPTIDF

SHO-VPTIDF used in the proposed photovoltaic system is demonstrated in Figure 3(a). The controller output is control signal ($u(t)$), while the input signal is error signal ($e(t)$). The Transfer Function (TF) for the SHO-VPTIDF is expressed as (Patra et al., 2020; Rath et al., 2021; Patra et al., 2022), similar to Equation (46)

$$TF = (K_t \times s^n) + K_d \left(\frac{N_3 \times s^\gamma}{N_3 + s^\gamma} \right) + \frac{K_a \times N_2 \times N_1 \times s^{\alpha+\beta}}{(s^\alpha + N_1)(s^\beta + N_2)} \quad (46)$$

where the tilt gain is represented by K_t acceleration gain K_a , derivative gain K_d , coefficient of tilt n , pre-filter gains N_1 , N_2 , and N_3 coefficient of accelerations α , β , and coefficient of derivative γ . The suggested model reacts to the fitness function (Integral Time Absolute Error (ITAE) and the lowest value is employed to evaluate the control parameters. The mathematical equivalence of ITAE is highlighted by Equation (47). In the proposed model, better performance including a lower harmonic content and a higher system voltage is caused by the lowest value of the fitness function.

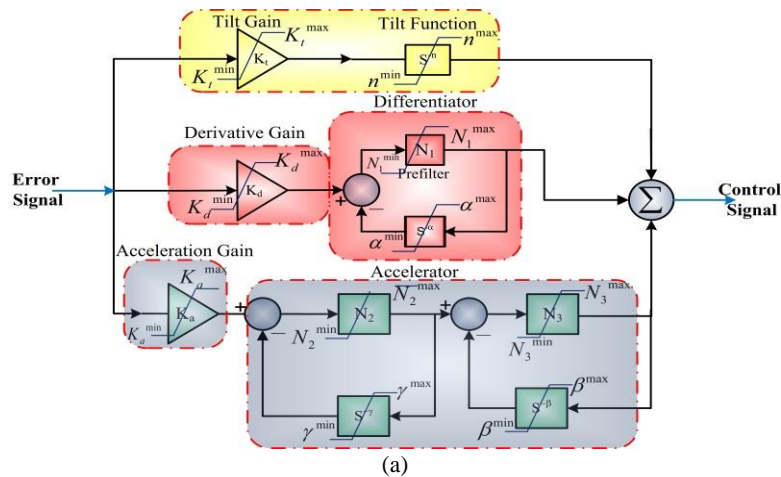
$$ITAE = \int_0^{\infty} |e(t)| \times t \times dt \quad (47)$$

where $|e(t)|$ denotes the error signal magnitude. The control parameters are estimated with the help of the SHO strategy in an effort to improve the performance of the photovoltaic system (Dhiman & Kumar, 2017). SHO has the capability to provide the best optimal solutions to the optimization problem. The optimization (SHO) is achieved through abatement in cost function (ITAE). The advantages of SHO like greater accuracy, greater probability, simplicity in implementation, high convergence power, simplicity in equations, and best outcome with the capability to avoid local optima proclaim its preeminence over most optimization techniques.

The control parameters for grid-connected photovoltaic systems are estimated using the SHO approach in order to control the output voltage (V_{inv}). The optimization variables have been selected to support determining the best settings for the VPTIDF controller. Table 1 represents the parameters of the SHO optimization approach. The optimization is carried out till the stopping criterion (maximum iteration) is reached. The optimal values of control parameters are adopted from the optimized results based on the lowest value of ITAE. The optimized values of control parameters along with their limits are placed in Table 2. The lower and upper bounds of the control parameters are obtained through optimization done individually by both methods. The block diagram of the SHO-VPTIDF control technique is shown in Figure 3(a). The working principle of SHO is clearly described by the aid of the flowchart represented in Figure 3(b).

Table 1. Optimization parameters for SHO

Number of search agents	30
Control parameter (random vector-1)	[5,0]
Random variable constant	[0.5,1]
Number of generations	1000



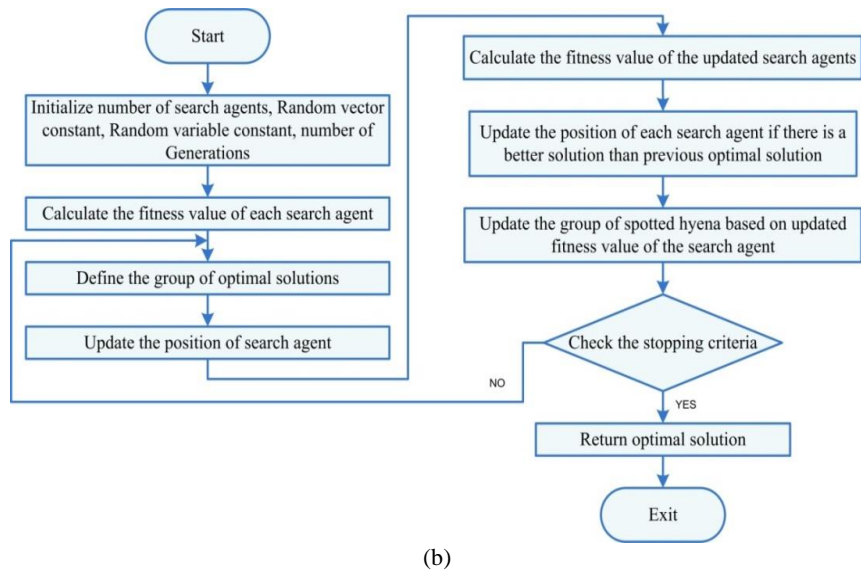


Figure 4. (a) Schematic representation of SHO-VPTIDF, (b) Flow chart of SHO

4. RESULTS AND DISCUSSION

The objectives of this section are to examine the results of the SHO-VPTIDF-based photovoltaic model and to demonstrate how the proposed strategy has improved in terms of performance, robustness, and stability.

4.1. Control action

The analysis of control parameter sensitivity justifies the control action of the proposed controller.

4.1.1. Control parameter sensitivity analysis

The settings of the controller affect the system performance. Thus, a control parameter setting is of significant importance (Dhiman & Kumar, 2017). The optimization technique employs the fitness function to optimize control parameters, but the response is not optimized. Control parameters are considered as constants and the controllers tend to present poor robustness and maximize rise time. The optimization of response or robustness is achieved by allowing control parameters to vary depending on the error. The error signal ($f(e)$) can be expressed mathematically in Equation (48).

$$F(e) = \frac{\sqrt{2}}{\sqrt{\pi}} \int_0^t e^{-\frac{t^2}{2}} dt \quad (48)$$

The SHO regulated VPFOTDAF is modeled for variation of control parameters. The variation of control parameters aims to give a better disturbance rejection ability, fast system response, and reduced overlapping. The upper and lower ranges of control parameters are presented in Table 2. The rapid response with decreasing settling time is achieved based on the tilt gain. Improper tuning has a tendency to increase system oscillations. The parametric variation of tilt gain is plotted in Figure 5(a). Reduction in the magnitude of steady state error is achieved by using acceleration, coefficient of tilt, and derivative gain. However, improper margins tend to induce rapid oscillations and overshoot. The acceleration, coefficient of tilt, and derivative gain parameter variations are plotted in Figure 5(a). The coefficient of acceleration and derivative facilitate proper tuning of the controller and disturbance rejection. The variation of the coefficient of acceleration and derivative is plotted in Figure 5(b). The disturbance present in the response of SHO regulated VPFOTDAF controller is achieved using a low-pass filter. The low-pass filter is implemented by using prefilter gains (N_1 , N_2 , and N_3). The parametric variation of prefilter gains (N_1 , N_2 , and N_3) is presented in Figure 5(c). The variation of V_b is presented in Figure 5(d). The variation in V_b is 0.20 volts, which is 0.44 %.

Table 2. The optimized control parameter values along with upper and lower bounds

Parameter	Indices name	Lower limit	Indices name	Upper limit	Optimized values
K_t	K_t^{\min}	0.2692	K_t^{\max}	0.538	0.2791
K_a	K_a^{\min}	0.2174	K_a^{\max}	0.3812	0.3333
K_d	K_d^{\min}	0.3801	K_d^{\max}	0.6462	0.4945
n	n^{\min}	0.2712	n^{\max}	0.70712	0.5054
α	α^{\min}	0.6192	α^{\max}	0.8462	0.7174
β	β^{\min}	0.1082	β^{\max}	0.594	0.4055
γ	γ^{\min}	0.14	γ^{\max}	0.3319	0.2311
N_1	N_1^{\min}	68.654	N_1^{\max}	225.659	123.8861
N_2	N_2^{\min}	44.68	N_2^{\max}	189.678	99.87
N_3	N_3^{\min}	234.648	N_3^{\max}	296.38	271.12

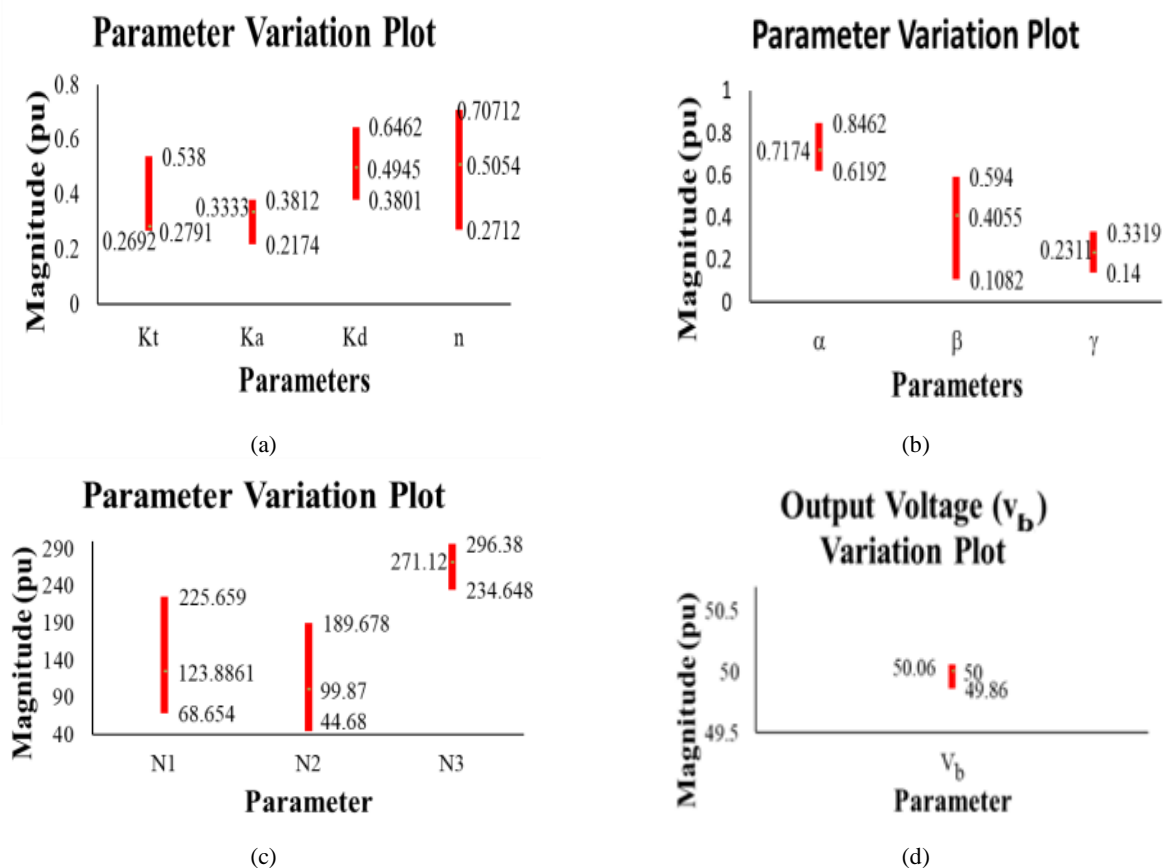


Figure 5. (a) The variation of K_t , K_a , K_d , and n , (b) variation of α , β , and γ , (c) variation of N_1 , N_2 , and N_3 , (d) variation of V_b with the modification of control parameters

4.2. Closed loop boost converter

The low voltage from solar panels lacks direct utilization. Thus, necessary measures need to be in place to heighten the magnitude from the solar panels. This enhancement is achieved by use of NBC. The switches in NBC are switched at 370 KHz by the VPTIDF controller. Figure 6 represents the output voltage from the NBC. In low-rating converters, the average value of output voltage is 48 volts. For low-rating converters, 50 volts is a serious output. Thus, to achieve enhanced performance, the NBC is designed to give an output voltage of 50 volts.

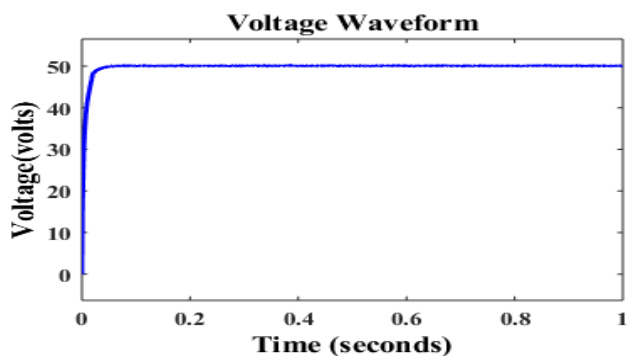


Figure 6. DC voltage output of the boost converter

4.3. Closed loop micro inverter

The micro inverter inverts the stepped-up DC voltage into AC. A load having an impedance of $100+240e-3j \Omega$ is connected

across the micro inverter. Micro inverter provides an inverted voltage of 220 volts, load current of 2 ampere, and power consumed by the load, which is of 360 watt. Figures 7-9 represent the inverted voltage, load current, and power consumed by load.

A three-terminal transformer connected to both the grid and proposed solar photovoltaic system (solar Micro Inverter) feeds the load of 12 KW. Figure 10 shows the contribution of the grid, proposed solar photovoltaic system, and the consumption of energy from the load. The magnitude of RMS voltage supplied by both the grid and inverter is 162.5 volts, while grid delivers a current of 6.3 ampere and a current of 11.63 ampere fed by the inverter. The voltage across the load is 169.5 volts with a current of 8.134 ampere.

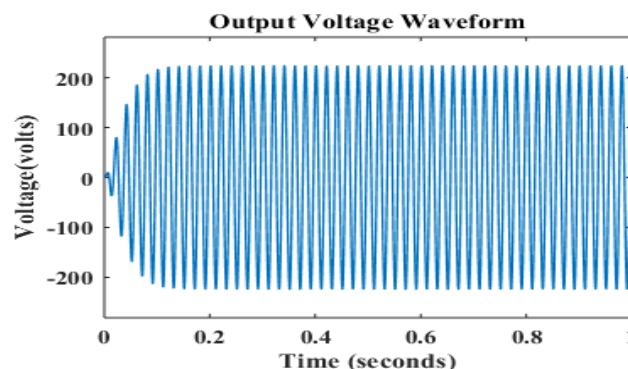


Figure 7. Output voltage of micro inverter

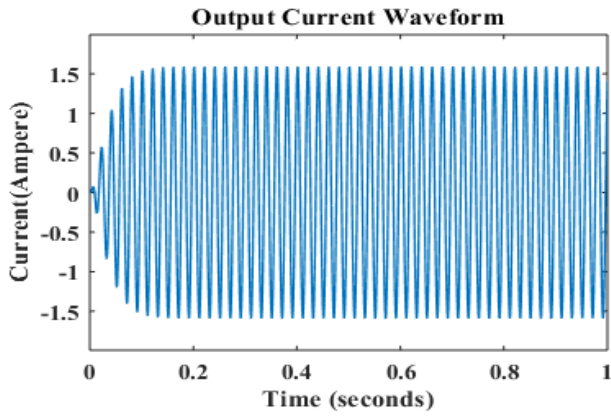


Figure 8. Output current of micro inverter

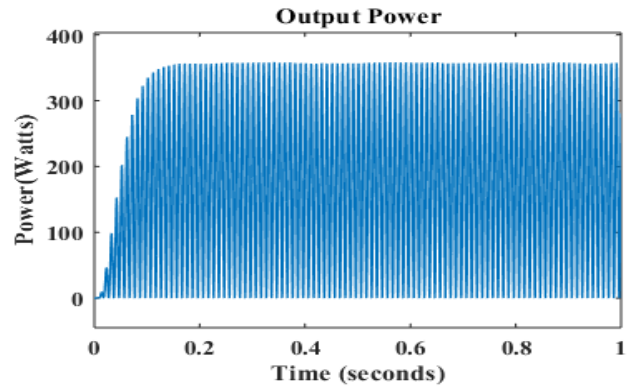


Figure 9. Output power of micro inverter

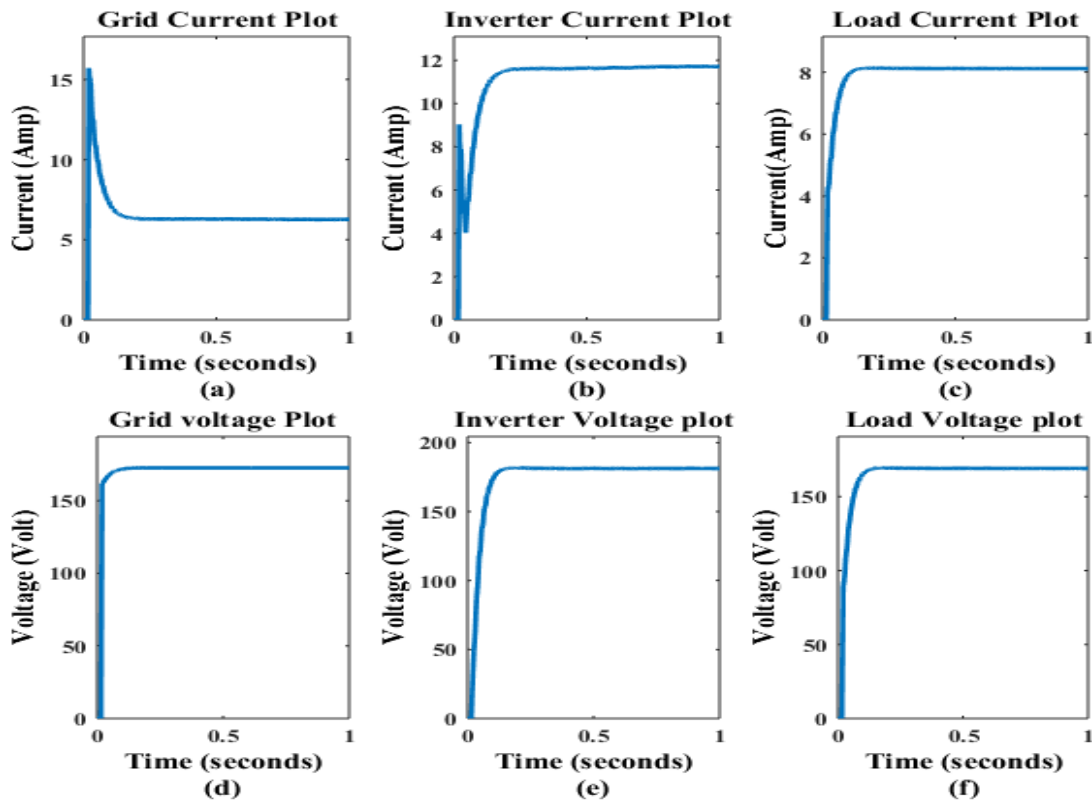


Figure 10. (a) Current supplied by grid, (b) Current supplied by Micro Inverter, (c) Current consumed by load connected, (d) Voltage supplied by grid, (e) Voltage supplied by Micro Inverter, (f) Voltage consumed by load connected

4.4. Closed loop fault analysis

The closed loop system is subjected to converter device fault at 0.2 second, load fault at 0.3 second, inverter device fault at 0.4 second, and grid fault at 0.5 second. RMS values of V_{inv} , i_{nv} , V_b , i_{load} , i_{grid} , V_{load} , V_{grid} , i_{rr} , T , $freq.$, i_b , i_{thd} , V_t , and I_t are the inputs to the LMA classifier. The impact of fault on

a closed loop system is evident in Figure 11. The closed loop system had minor impact of fault on the proposed photovoltaic system. It clearly shows that the photovoltaic system, when connected in the closed loop condition, is able to recover from the fault and its performance is not impacted by the presence of faults. Due to the ability of adaptive optimal control technique (SHO-VPTIDF) to self-adjust, the effects of faults on the system output are kept to a minimum.

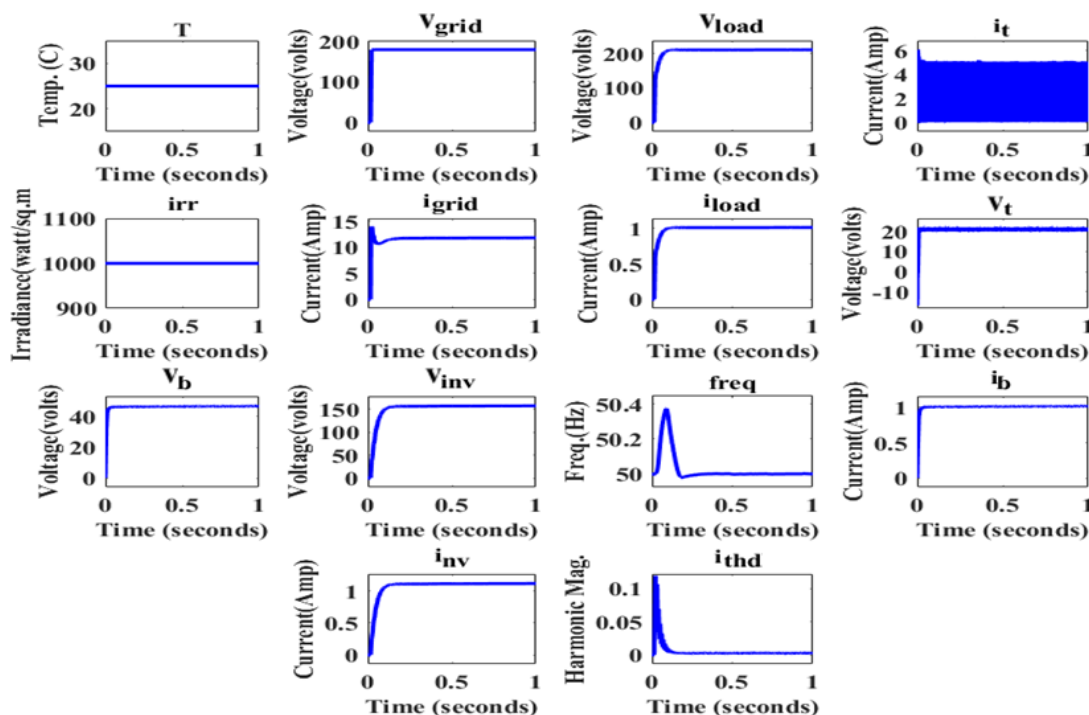


Figure 11. Fault analysis of the closed-loop system

4.5. Robustness analysis

The ability to endure rapid or abnormal change in operating conditions is called the robustness of the system. The operating conditions of the proposed photovoltaic system are irradiance and temperature. The robustness is verified if the change in operating conditions do not impact the system responses. The robustness of the proposed photovoltaic system is analyzed for changes in the voltage, current, and power of micro inverter. The optimal operating range of temperatures for photovoltaic activity is from 20 °C to 48 °C. The deviation in the RMS value is from 160.98 volts to 161.24 volts, as represented in Figure 12(a). This deviation of 0.26 volts amounts to 0.162 % variation from the full load. The deviation for the output current from the micro inverter is between 1.4125 amp and 1.4135 ampere. This deviation in current of 0.001 amp amounts to 0.074 % variation from full load, as represented in Figure 12 (b). The variation in the output power of the micro inverter from full load is 0.645 %, as represented in Figure 12 (c). The variation is between 248.3 watts and 294.8 watts. The power per unit area is received from the sun on the horizontal surface at the sea level. The maximum value of irradiance is 1361 watt/square meter (W/M²). The variation in irradiance is from 700 W/M² to 1361 W/M². The irradiance range is chosen to be an optimal range for generation of voltage from photovoltaic panels. The output voltage of a micro inverter varies from 160.98 volts to 164.5 volts, as depicted in Figure 12 (d). This variation of 3.52 volts is 2.18 % from full load. Figure 12(e) represents the variation

of current from the micro inverter. This variation in the output current of the micro inverter is 0.003 amp (1.4125 amp to 1.4155 amp), which is 0.022 % of full load current. The deviation in power is of 10 watts (245 watt to 255 watt). The 4.03 % deviation in the output power of micro inverter is represented in Figure 12(f). The proposed system witnesses minute variations (within the tolerance level of 5 %) under large-scale fluctuations in operating conditions. The PV system is not prone to disturbances, thereby exhibiting robust characteristics.

Figure 13(a) to (b) shows the robustness of the open-loop and closed-loop systems under fault conditions to confirm the robustness. The open-loop mode (Figure 13(a)) shows that the system response is not robust. The parameters used to monitor the robustness are the RMS values of V_{inv} , i_{nv} , V_b , i_{load} , i_{grid} , V_{load} , V_{grid} , irr , T , $freq.$, i_b , i_{thd} , V_t , and I_t . When the proposed system is subjected to a fault and variation in temperature and irradiance, then it loses its robustness. Meanwhile, the closed loop system represented in Figure 13(b) shows its robust nature. It clearly shows that a closed-loop condition, the photovoltaic system is able to recover from the faults and its robust nature is not impacted by the presence of faults. Due to the ability of the adaptive optimal control technique (SHO-VPTIDF) to self-adjust, the effects of faults on the system output are kept to a minimum.

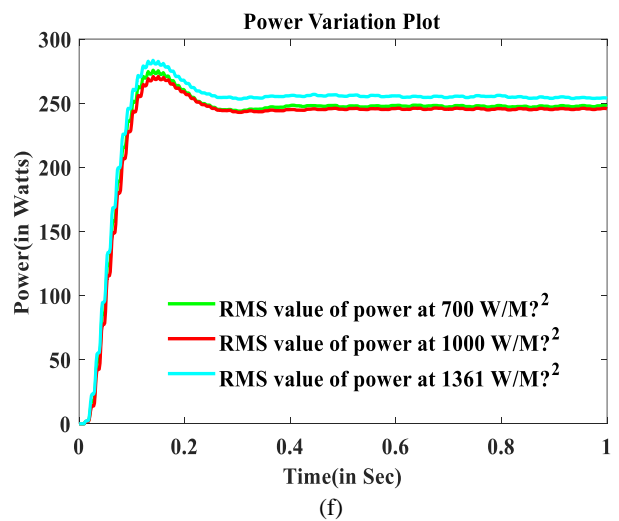
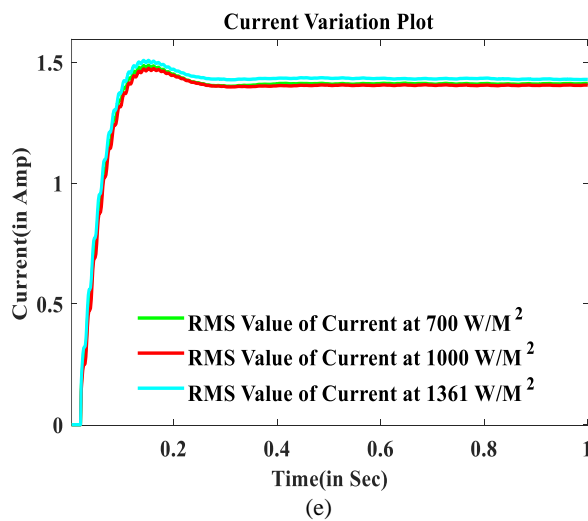
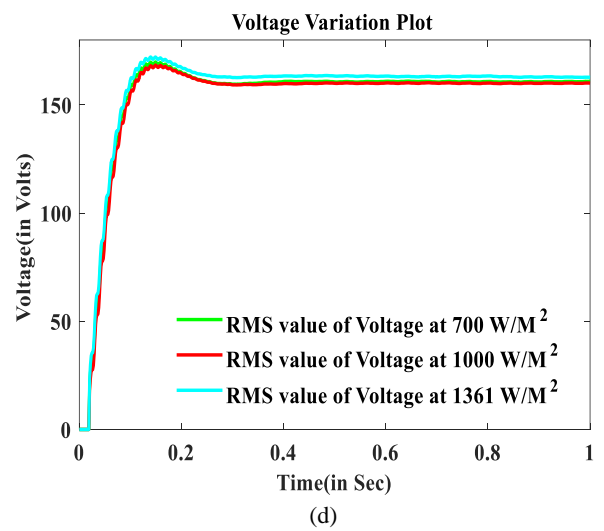
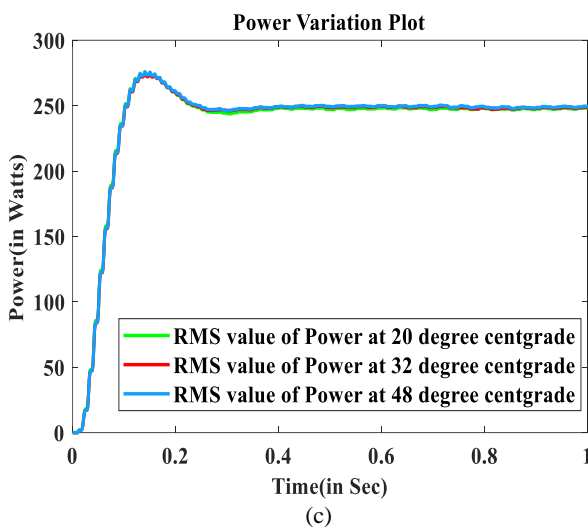
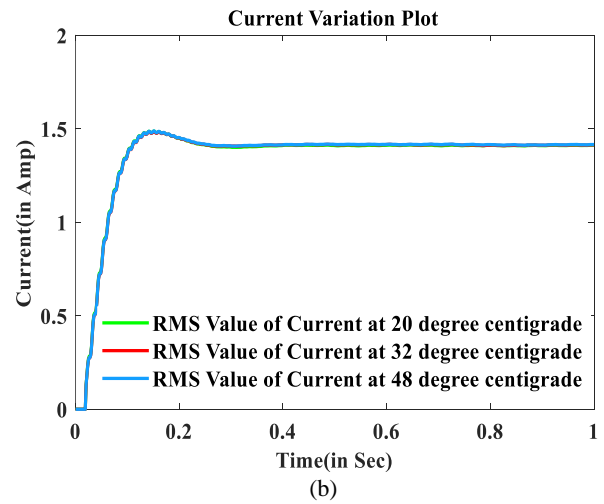
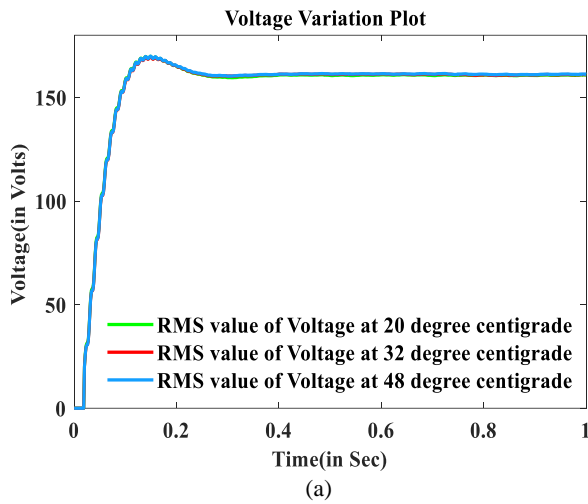


Figure 12. Performance of a micro inverter with variation in temperature: (a) Variation of output voltage, (b) Variation of output current, (c) Variation of output power, Performance of a micro inverter with variation in irradianc, (d) Variation of output voltage, (e) Variation of output current, (f) Variation of output power

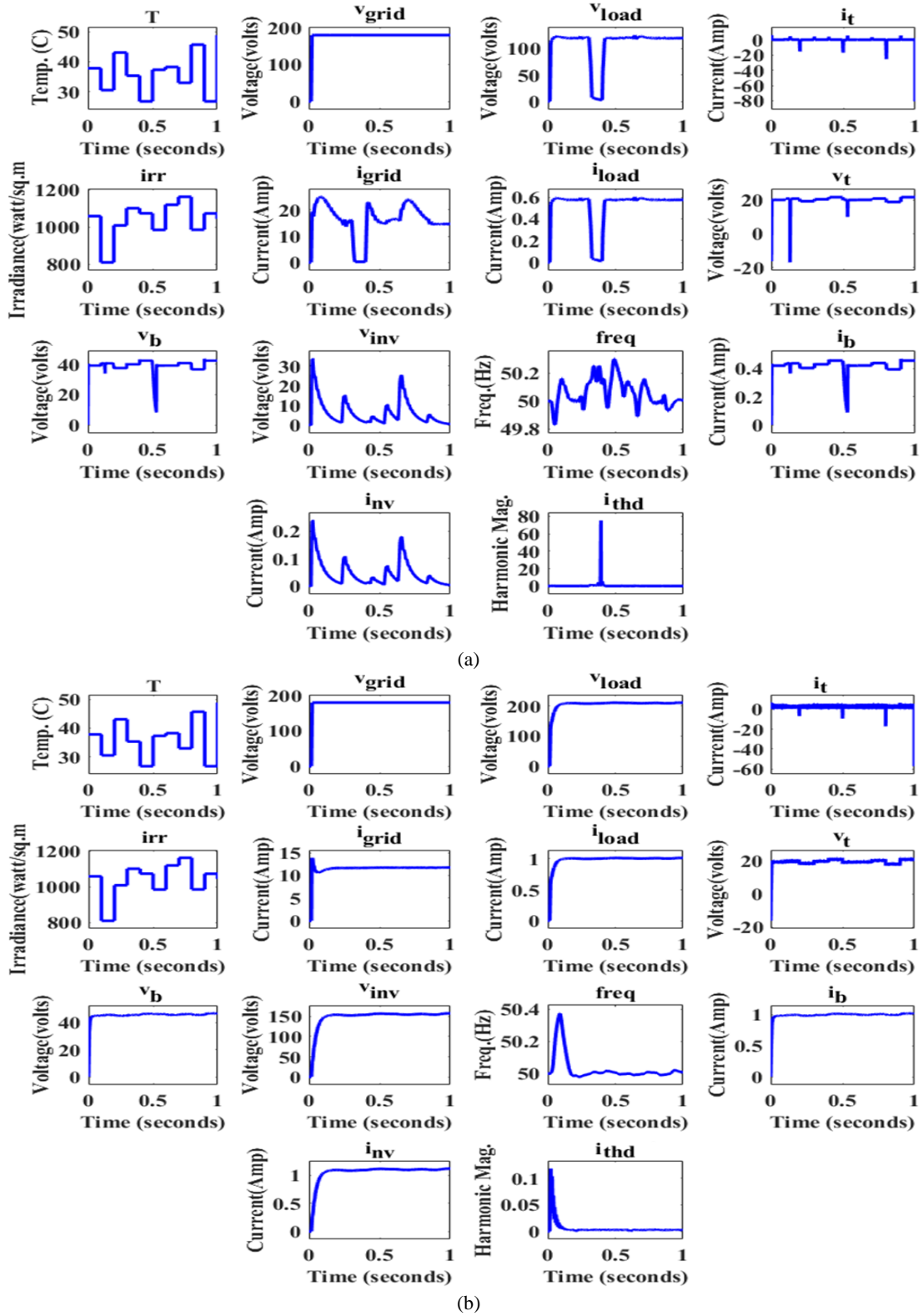


Figure 13. (a) Impact of fault on robustness analysis for the open-loop mode, (b) Impact of fault on robustness analysis for the closed-loop mode

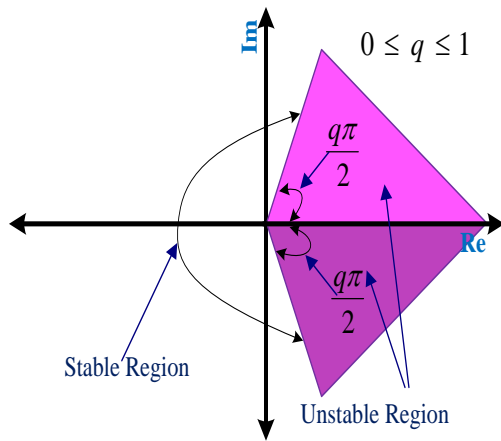
4.6. Stability of variable parameter tilt integral derivative with filter controller

The stability of the proposed model is validated using Matignon stability theorem (Ben Makhoul et al., 2020). The stability analysis of the proposed model is carried out in the frequency domain by using Matignon stability theorem. The roots of the characteristic equation of the linear time-invariant system should not be present on the left-hand side of the s-plane neither be far away from the origin. This is not the case with the dynamic system stability of fractional-order systems. Matignon

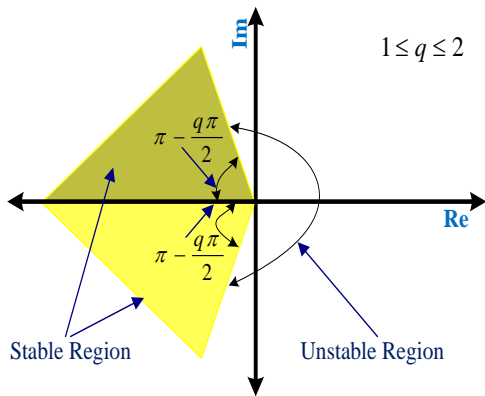
stability theorem states that a fractional-order system having a transfer function TF is stable if it complies with Equation (49). σ_i represents the i^{th} roots of the characteristic equation in the s-domain. The order of the fractional integral is represented by q .

$$\left| \arg(\sigma_i) \right| = q \frac{\pi}{2}, \left\{ \sigma = s^q : q \ni (0 \leq q \leq 2) : \forall \sigma_i \in \mathbb{C} \right\} \quad (49)$$

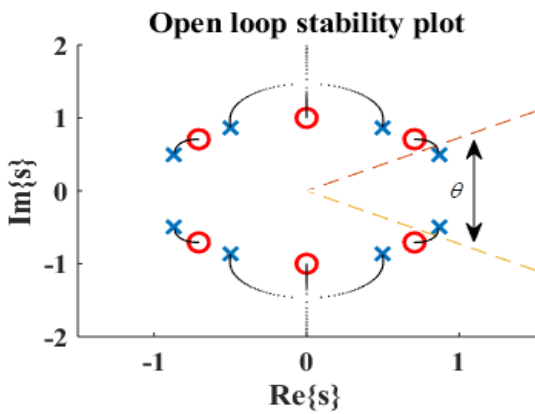
The dependence on the value of q in the stable region of fractional-order systems in s plane is either smaller or larger. If the value of q lies between 0 and 1, the stable region of fractional-order systems is very large. This is represented by Figure 14(a). If the value of q lies between 1 and 2, the stable region of fractional-order systems is very small, as represented by Figure 14(b). The open-loop response is represented by Figure 14(c). The stability plot for the proposed closed-loop SHO-VPTIDF system is represented in Figure 14(d) to (e). The proposed model is obviously stable because there are no poles or zeros at angle θ , whereas for an open-loop response, poles exist in an unstable region.



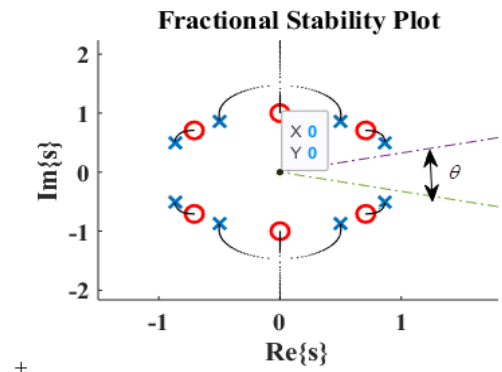
(a)



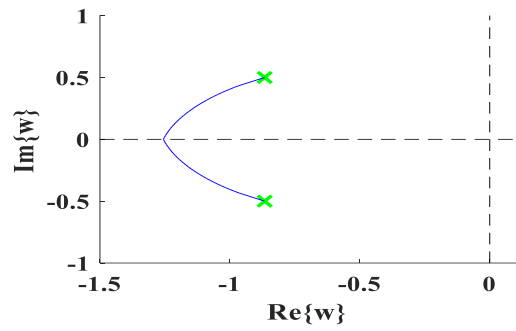
(b)



(c)



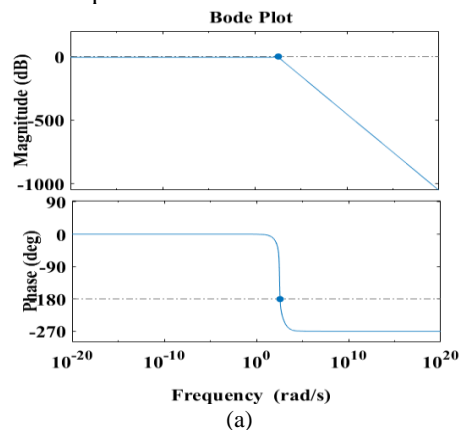
(d)



(e)

Figure 14. (a) Matignon stability plot for q values less than 1, (b) Matignon stability plot for q values more than 1 but less than 2, (c) Root locus plot for the photovoltaic system open-loop plot, (d) Root locus plot for photovoltaic system closed-loop SHO-VPTIDF plot for all s 's, (e) Root locus plot for the photovoltaic system closed-loop SHO-VPTIDF plot for all $s = j\omega$.

Bode plot is used for the analysis of impact of fault on the stability of the system. The impact of fault on stability is analyzed through the bode analysis of the proposed photovoltaic system. The bode plot under normal conditions, open-loop fault condition, and closed-loop fault condition is represented in Figure 15(a) to (c). It is evident from Figure 15(b) that when the open-loop system is subjected to fault, there is an apparent loss of stabilization, which is because of the inability of the system to restore its normal operating condition. Figure 15(c) represents the operating condition of SHO-VPTIDF solar photovoltaic system. It is evident from Figure 15(c) that there is a mild peak in the response of the system and the system has recovered from the fault. This is made possible by the adaptive optimal control technique (SHO-VPTIDF), which has the ability to adjust itself so that the impact of faults on the system output is minimized.



(a)

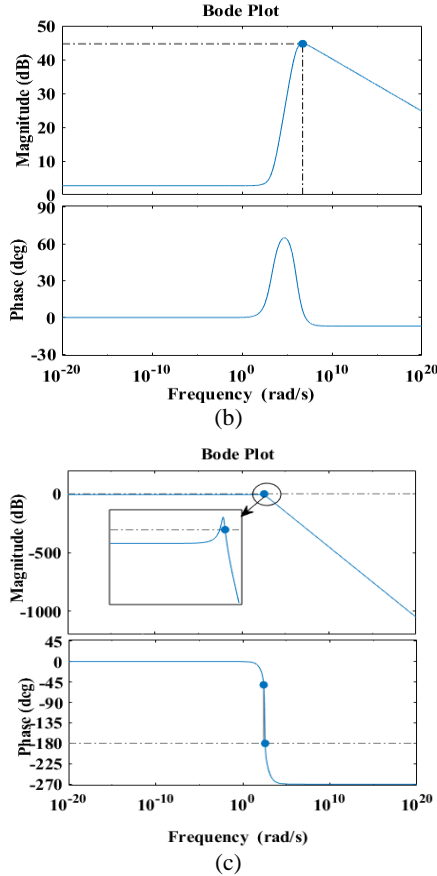


Figure 15. (a) Bode Plot for normal operating condition, (b) Bode plot under fault condition in the open-loop mode, (c) Bode plot under fault conditions in the closed-loop mode.

4.7. Fault classification

The performance analysis validation plot for LMA is represented by Figure 16(a). It is clear from the plot that the best performance of 1.3206×10^{-9} is attained at 953 epochs. The error histogram plot for LMA is represented in Figure 16(b). The plot suggests that the proposed fault detection technique has higher accuracy and precision given that the error is small. Table 3 highlights the LMA metrics.

Table 3. LMA parameters

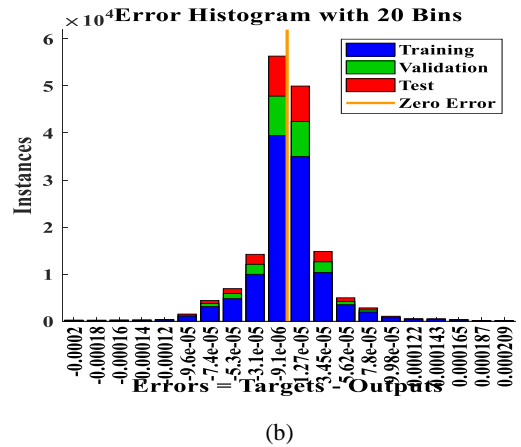
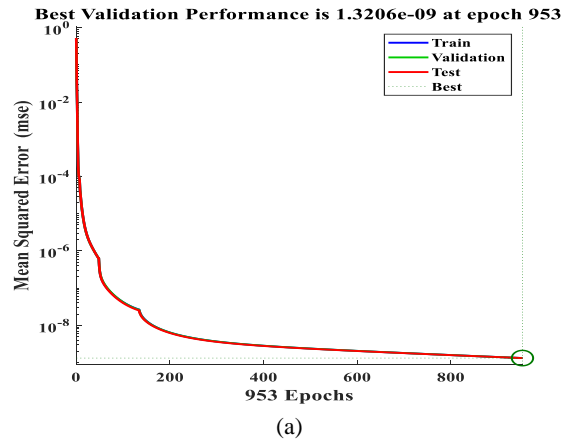
LMA	Samples	MSE	R
Training	112006	1.32166×10^{-9}	9.999999×10^{-1}
Validation	24001	1.32064×10^{-9}	9.999999×10^{-1}
Testing	24001	1.31941×10^{-9}	9.999999×10^{-1}

The frequency of recurring error is shown by the error histogram. There would be minor error when the training is appropriate with slightest inconsistencies. The training failure plot highlights the shortcomings of data training. A minimum or non-existent number of failures points to the best fit solution. The failures of the pool training are shown in Figure 16(c). The regression plot provides information about data scattering. It can have a value between -1 and 1, or between 0 and 1. Reverse fit is indicated by a value of -1, and perfect fit is indicated by a value of 1. No fit is indicated by a value of 0. In Figure 16(d), the regression plot is shown. V_{inv} , i_{nv} , V_b , i_{load} , i_{grid} , V_{load} , V_{grid} , irr , T , $freq.$, i_b , i_{thd} , V_1 , and I_1 the inputs to the

LMA based fault classifier. The three output determiners Y_1 , Y_2 , and Y_3 facilitate classifying the type of faults. Table 4 contains and highlights the specifics.

Table 4. Binary equivalence of various operating conditions

Y_1	Y_2	Y_3	Operating condition
0	0	0	Normal operating condition
0	0	1	Grid open circuit,
0	1	0	Grid short circuit
0	1	1	Load open circuit
1	0	0	Load short circuit
1	0	1	Inverter open circuit
1	1	0	Inverter fault
1	1	1	Converter fault



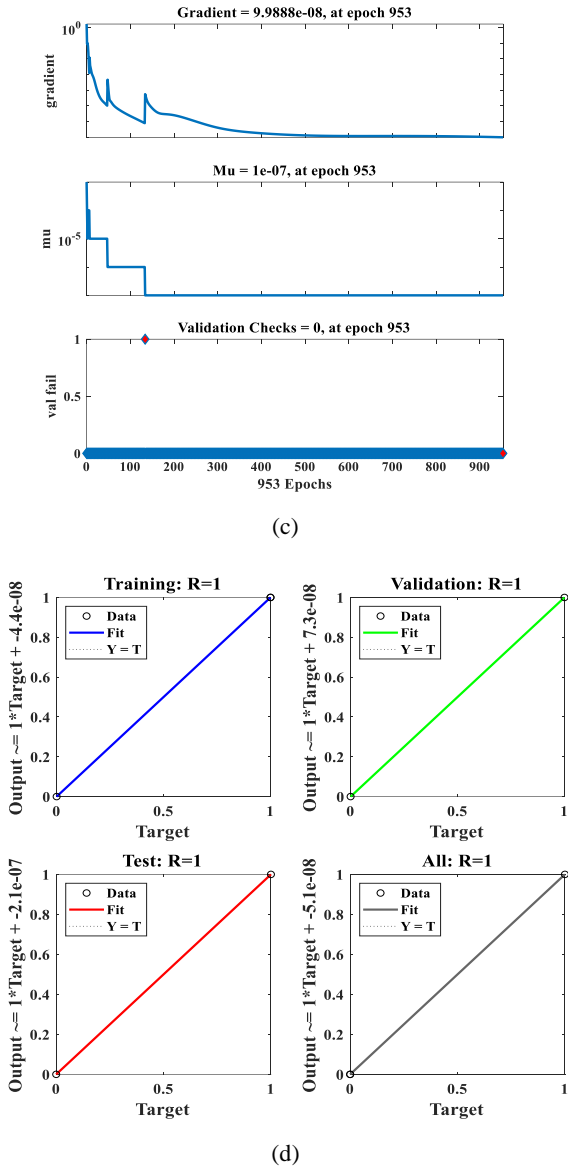


Figure 16. Performance exploration of LMA-based fault classifier: (a) Performance validation plot, (b) Error histogram analysis Plot, (c) Training validation analysis Plot, (d) Regression analysis Plot

The plot for the normal operating condition, known as the no-fault condition, is shown in Figure 17(a) to (c). The values of three output determiners Y_1 , Y_2 , and Y_3 are zero. The values of three output determiners Y_1 , Y_2 , and Y_3 are 0,0, and 1 in a grid open-circuit fault condition. The output determiners plot for grid open circuit fault are shown in Figure 17(d) to (f).

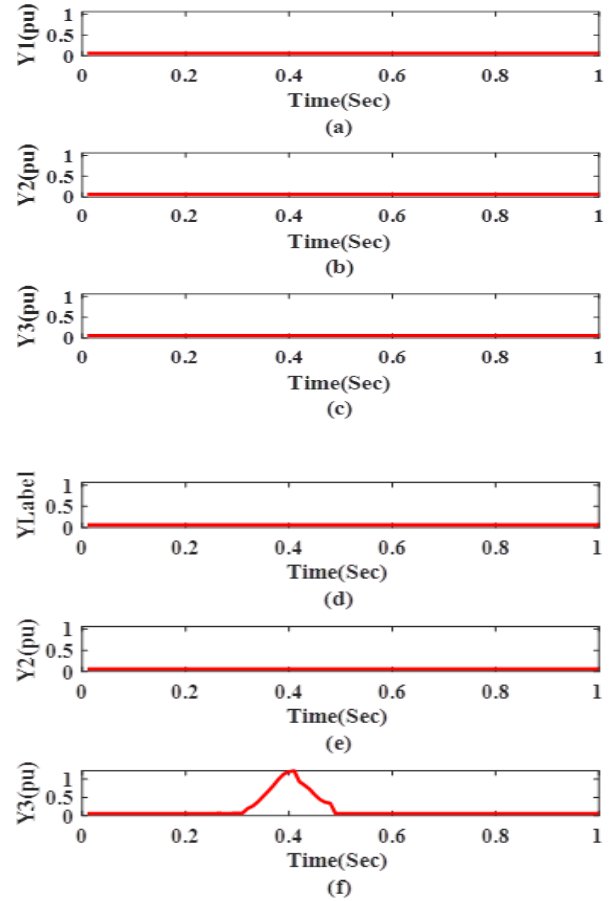
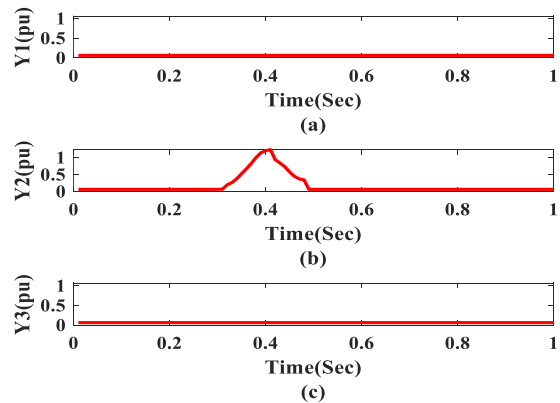
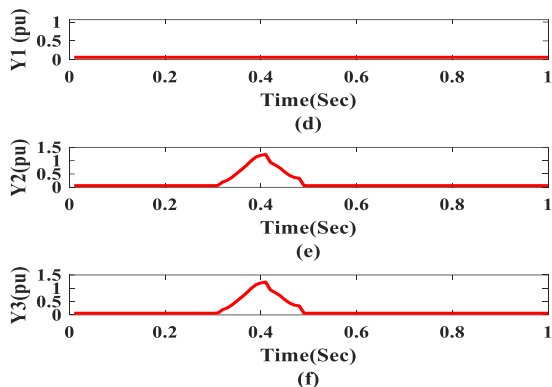


Figure 17. (a) Classification of normal conditions using the determiner (Y_1); (b) Classification of normal conditions using determiner (Y_2); (c) Classification of normal conditions using determiner (Y_3); (d) Classification of Grid open circuit fault conditions using determiner (Y_1); (e) Classification of grid open circuit fault conditions using determiner (Y_2); (f) Classification of grid open circuit fault conditions using determiner (Y_3)

The output variables of grid short circuit under faulty conditions are $Y_1 = 0$, $Y_2 = 1$, and $Y_3 = 0$. This is represented in Figure 18(a-c). Figure 18(d) to (f) represents the load open-circuit faulty conditions. The output variables of load open circuit faulty conditions are $Y_1 = 0$ and $Y_2 = Y_3 = 1$.





inverter open circuit fault conditions using determiner (Y_1); (e) Classification of inverter open circuit fault conditions using determiner (Y_2); (f) Classification of inverter open circuit fault conditions using determiner (Y_3)

The values of three output determiners Y_1 , Y_2 , and Y_3 are 1, 0, and 0 in a inverter fault condition. The output determiners plot for inverter fault is shown in Figure 20(a) to (c). The values of three output determiners Y_1 , Y_2 , and Y_3 are 1, 0, and 1 in the converter open circuit fault condition. The plot of output determiners for the converter open circuit fault is shown in Figure 20(d) to (f).

Figure 18. (a) Classification of grid short circuit fault conditions using determiner (Y_1); (b) Classification of grid short circuit fault conditions using determiner (Y_2); (c) Classification of grid short circuit fault conditions using determiner (Y_3); (d) Classification of load open circuit fault conditions using determiner (Y_1); (e) Classification of load open circuit fault conditions using determiner (Y_2); (f) Classification of load open circuit fault conditions using determiner (Y_3)

The values of three output determiners Y_1 , Y_2 , and Y_3 are 1, 0, and 0 in a load short fault condition. The plot of output determiners for load short fault is shown in Figure 19(a) to (c). The values of three output determiners Y_1 , Y_2 , and Y_3 are 1, 0, and 1 in an inverter open circuit fault condition. The output determiners plot for inverter open circuit fault are shown in Figure 19(d) to (f).

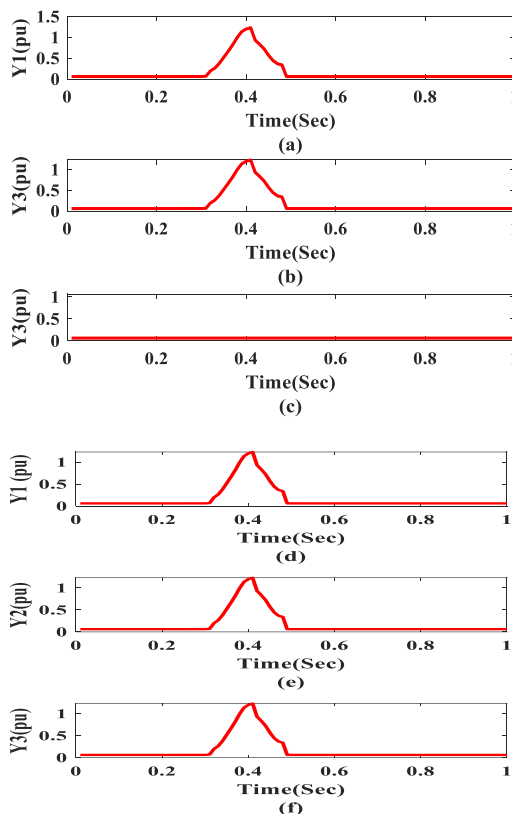


Figure 20. (a) Classification of inverter fault conditions using the output determiner (Y_1); (b) Classification of inverter fault conditions using the output determiner (Y_2); (c) Classification of inverter fault conditions using the output determiner (Y_3); (d) Classification of converter fault conditions using the output determiner (Y_1); (e) Classification of converter fault conditions using the output determiner (Y_2); (f) Classification of converter fault conditions using the output determiner (Y_3)

Rapid and effective fault detection is essential for fault mitigation. Here, a 5-cycle fault duration was selected. There are 50 cycles in a second at a frequency of 50 Hz. Five cycles must be completed in 0.1 seconds. The duration of fault was set at 0.1 seconds since that is the shortest possible time for any faulty condition. Small duration faults are used to test the classifier. The classifier takes 0.015 seconds to detect the fault following the occurrence of a fault.

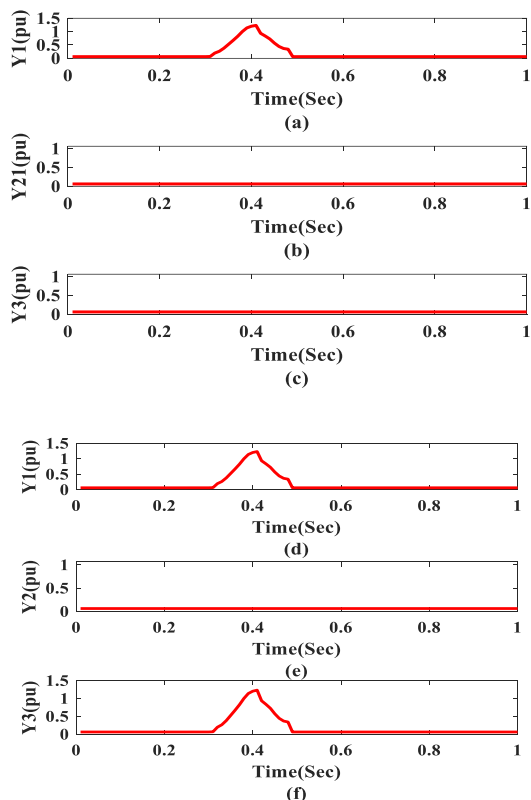


Figure 19. (a) Classification of load short circuit fault conditions using determiner (Y_1); (b) Classification of load short circuit fault conditions using determiner (Y_2); (c) Classification of load short circuit fault conditions using determiner (Y_3); (d) Classification of

4.8. Comparative analysis

The comparative study of the proposed SHO-VPTIDF-based photovoltaic system and other modern controllers displays the superiority of the former, as presented in Table 5. IEEE sets the benchmark to approve a novel technique. According to IEEE-519, for a period of 30 cycles the total harmonics must be less than 5 %. The proposed model delivers the current harmonic to be 0.27 % and voltage harmonics of 0.52 %, as presented in Figure 21.

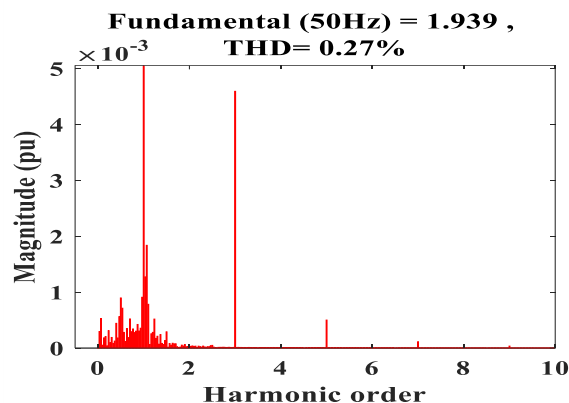


Figure 21. Current harmonic plot for the proposed system

Table 5. Comparative study of SHO-VPTIDF controller based Photovoltaic system with other modern control techniques in terms of performance

Criteria	Solar-photovoltaic model with HCC (Keddar et al., 2019)	Solar-photovoltaic model with PRC (Ahmad & Singh, 2017)	Solar-photovoltaic model with PRDC (Huang et al., 2018)	Solar-photovoltaic model with SOGI-PLL (Zeb et al., 2019)	Solar-photovoltaic model with HB-SPWM (Zhao et al., 2018)	Solar-photovoltaic model with PLL-FF (Wang et al., 2020)	Solar-photovoltaic model with SHO-VPTIDF
i_{thd}	2.35 %	2.1 %	1.79 %	1.55 %	1.16 %	1.1 %	0.27 %
SPWM	SVPWM	Bipolar SPWM	Multi frequency PWM	SPWM	SPWM	SPWM	DQCSPWM
Switching frequency	15 KHz	10 KHz	10 KHz	10 KHz	10 KHz	20 KHz	8.5 KHz
Stability	Mediocre	Mediocre	Mediocre	Mediocre	Mediocre	Mediocre	Superior
Robust	Mediocre	Mediocre	Mediocre	Mediocre	Mediocre	Mediocre	Superior
Fault classification ability	Negative	Negative	Negative	Negative	Negative	Negative	Affirmative

5. CONCLUSIONS

SHO-VPTIDF, a novel control strategy, was proposed based on variable fractional-order controller concepts. The novelty of the proposed strategy included improved stability, better robustness, upgraded accuracy, better harmonic mitigation ability, and improved ability to handle uncertainties and they were verified in a MATLAB Simulink environment. The simulation result justified the use of variable SHO-VPTIDF and DQCSPWM given improved ability to eliminate harmonics as well as the robustness and stability of the overall system. Any system will have faults. It was believed that the fault detection mechanism used by machine learning techniques would be strong enough to identify the fault. This finding was supported by simulated outcomes. The obtained results validated the real-time implementation of the strategy due to its enhanced performance, fault detection capability, robustness, and stability of variable SHO-VPTIDF along with DQC-based SPWM technique.

6. CONTRIBUTORSHIP

All the authors have contributed equally to the design and implementation of the research, to the analysis of the results and to the writing of the manuscript.

7. ACKNOWLEDGEMENT

The authors would like to acknowledge and appreciate Siksha 'O' Anusandhan University for their support. This research received no funding.

REFERENCES

- Ahmad, Z., & Singh, S. N. (2017). Comparative analysis of single phase transformerless inverter topologies for grid connected PV system. *Solar Energy*, 149(1), 245-271. <https://doi.org/10.1016/j.solener.2017.03.080>
- Ben Makhlof, A., Boucenna, D., & Hammami, M. A. (2020). Existence and stability results for generalized fractional differential equations. *Acta Mathematica Scientia*, 40(1), 141-154. <https://doi.org/10.1007/s10473-020-0110-3>
- Chaithanakulwat, A., Thungsuk, N., Savangboon, T., Boontua, S., & Sardyoung, P. (2021). Optimized DQ vector control of single-phase grid-connected inverter for photovoltaic system. *Journal Européen des Systèmes Automatisés*, 54(1), 45-54. <https://doi.org/10.18280/jesa.540106>
- Dhiman, G., & Kumar, V. (2017). Spotted hyena optimizer: a novel bio-inspired based metaheuristic technique for engineering applications. *Advances in Engineering Software*, 114(1), 48-70. <https://doi.org/10.1016/j.advengsoft.2017.05.014>
- Fazai, R., Abodayeh, K., Mansouri, M., Trabelsi, M., Nounou, H., Nounou, M., & Georghiou, G. E. (2019). Machine learning-based statistical testing hypothesis for fault detection in photovoltaic systems. *Solar Energy*, 190(1), 405-413. <https://doi.org/10.1016/j.solener.2019.08.032>
- Hu, X., Ma, P., Wang, J., & Tan, G. (2019). A hybrid cascaded DC-DC boost converter with ripple reduction and large conversion ratio. *IEEE Journal of Emerging and Selected Topics in Power Electronics*, 8(1), 761-770. <https://doi.org/10.1109/JESTPE.2019.2895673>
- Huang, K. P., Wang, Y., & Wai, R. J. (2018). Design of power decoupling strategy for single-phase grid-connected inverter under nonideal power grid. *IEEE Transactions on Power Electronics*, 34(3), 2938-2955. <https://doi.org/10.1109/TPEL.2018.2845466>
- Keddar, M., Doumbia, M. L., Krachai, M. D., Belmokhtar, K., & Midoun, A. H. (2019). Interconnection performance analysis of single phase neural network based NPC and CHB multilevel inverters for grid-connected PV systems. *International Journal of Renewable Energy Research*, 9(3), 1451-1461. <https://doi.org/10.20508/ijrer.v9i3.9593.g7730>
- Khan, M. N. H., Forouzesh, M., Siwakoti, Y. P., Li, L., Kerekes, T., & Blaabjerg, F. (2019). Transformerless inverter topologies for single-phase photovoltaic systems: A comparative review. *IEEE Journal of*

- Emerging and Selected Topics in Power Electronics*, 8(1), 805-835.
<https://doi.org/10.1109/JESTPE.2019.2908672>
10. Marrero, L., García-Santander, L., Hernandez-Callejo, L., Bañuelos-Sánchez, P., & González, V. J. (2021). Harmonic distortion characterization in groups of distribution networks applying the IEEE Standard 519-2014. *IEEE Latin America Transactions*, 19(4), 526-533.
<https://doi.org/10.1109/TLA.2021.9448534>
 11. Missula, J. V., Adda, R., & Tripathy, P. (2021). Averaged modeling and SRF-based closed-loop control of single-phase ANPC inverter. *IEEE Transactions on Power Electronics*, 36(12), 13839-13854.
<https://doi.org/10.1109/TPEL.2021.3083279>
 12. Mokhtar, M., Marei, M. I., & Attia, M. A. (2021). Hybrid SCA and adaptive controller to enhance the performance of grid-connected PV system. *Ain Shams Engineering Journal*, 12(4), 3775-3781.
<https://doi.org/10.1016/j.asej.2021.03.019>
 13. Patra, A. K., & Rout, P. K. (2020). Design of artificial pancreas based on the SMGC and self-tuning PI control in type-I diabetic patient. *International Journal of Biomedical Engineering and Technology*, 32(1), 1-35.
<https://doi.org/10.1504/IJBET.2020.104675>
 14. Patra, A. K., Biswal, S. S., & Rout, P. K. (2022). Backstepping linear quadratic gaussian controller design for balancing an inverted pendulum. *IETE Journal of Research*, 68(1), 150-164.
<https://doi.org/10.1080/03772063.2019.1592716>
 15. Rath, D., Patra, A. K., & Kar, S. K. (2021). Riddance and harmonic characterisation of photovoltaic fed single phase h-cascaded multilevel inverter. *International Journal of Advanced Mechatronic Systems*, 9(3), 133-145.
<https://doi.org/10.1504/IJAMECHS.2021.119107>
 16. Sadaf, S., Bhaskar, M. S., Meraj, M., Iqbal, A., & Al-Emadi, N. (2020). A novel modified switched inductor boost converter with reduced switch voltage stress. *IEEE Transactions on Industrial Electronics*, 68(2), 1275-1289.
<https://doi.org/10.1109/TIE.2020.2970648>.
 17. Sattianadan, D., Gorai, S., Kumar, G. P., Vidyasagar, S., & Shanmugasundaram, V. (2020). Potency of PR controller for multiple harmonic compensation for a single-phase grid connected system. *International Journal of Power Electronics and Drive Systems*, 11(3), 1491-1499.
<https://doi.org/10.11591/ijpeds.v11.i3.pp1491-1498>
 18. Tzounas, G., Dassios, I., Murad, M. A. A., & Milano, F. (2020). Theory and implementation of fractional order controllers for power system applications. *IEEE Transactions on Power Systems*, 35(6), 4622-4631.
<https://doi.org/10.1109/TPWRS.2020.2999415>
 19. Wang, X., Qin, K., Ruan, X., Pan, D., He, Y., & Liu, F. (2020). A robust grid-voltage feedforward scheme to improve adaptability of grid-connected inverter to weak grid condition. *IEEE Transactions on Power Electronics*, 36(2), 2384-2395.
<https://doi.org/10.1109/TPEL.2020.3008218>
 20. Xu, J., Qian, Q., Zhang, B., & Xie, S. (2019). Harmonics and stability analysis of single-phase grid-connected inverters in distributed power generation systems considering phase-locked loop impact. *IEEE Transactions on Sustainable Energy*, 10(3), 1470-1480.
<https://doi.org/10.1109/TSTE.2019.2893679>
 21. Yaqoob, S. J., Obed, A., Zubo, R., Al-Yasir, Y. I., Fadhel, H., Mokryani, G., & Abd-Alhameed, R. A. (2021). Flyback photovoltaic micro-inverter with a low cost and simple digital-analog control scheme. *Energies*, 14(14), 4239-4251.
<https://doi.org/10.3390/en14144239>
 22. Zeb, K., Islam, S. U., Din, W. U., Khan, I., Ishfaq, M., Busarello, T. D. C., ... & Kim, H. J. (2019). Design of fuzzy-PI and fuzzy-sliding mode controllers for single-phase two-stages grid-connected transformerless photovoltaic inverter. *Electronics*, 8(5), 520-539.
<https://doi.org/10.3390/electronics8050520>
 23. Zhao, H., Wang, S., & Moeini, A. (2018). Critical parameter design for a cascaded H-bridge with selective harmonic elimination/compensation based on harmonic envelope analysis for single-phase systems. *IEEE Transactions on Industrial Electronics*, 66(4), 2914-2925.
<https://doi.org/10.1109/TIE.2018.2842759>